iScience

CellPress
OPEN ACCESS

Article

A High-Performance Aqueous Zinc-Bromine Static Battery

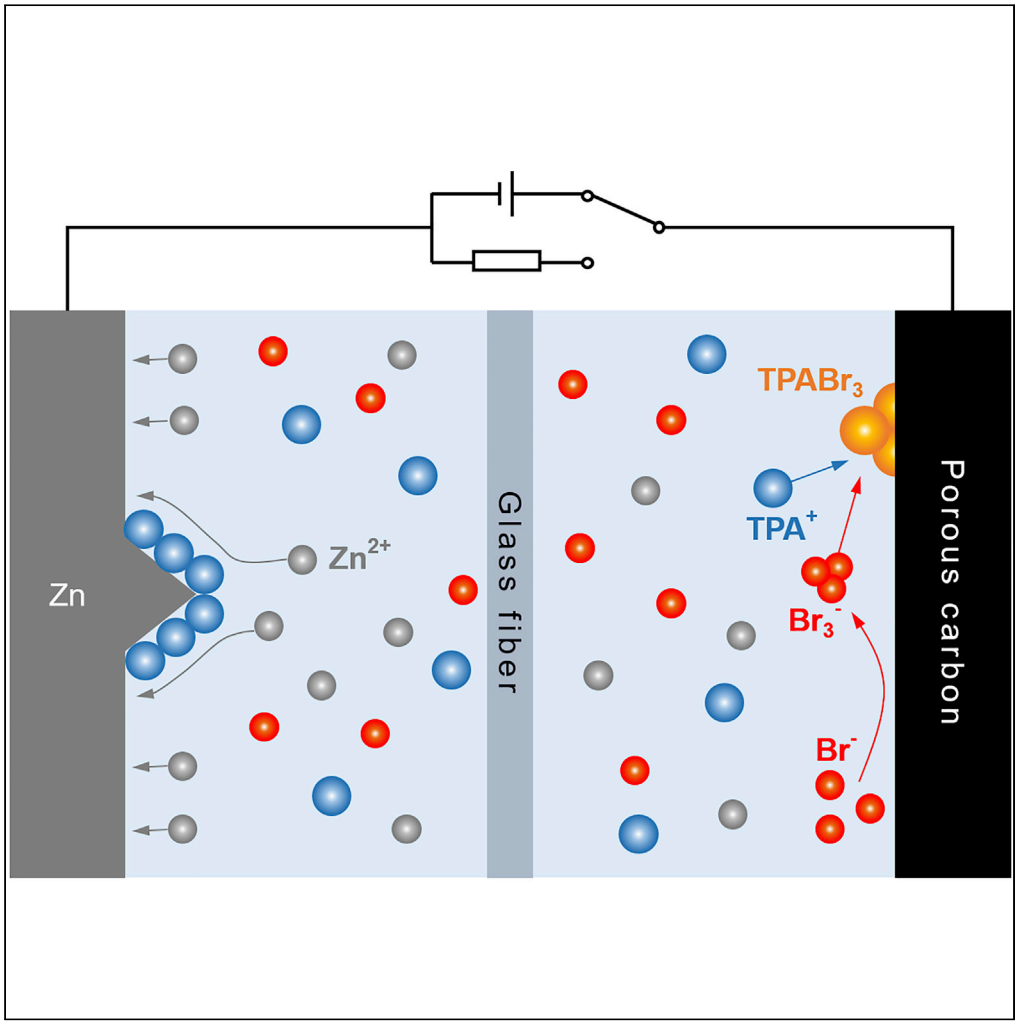

Lujie Gao, Zhuxin Li, Yiping Zou, Shuangfeng Yin, Peng Peng, Yuying Shao, Xiao Liang

xliang@hnu.edu.cn

HIGHLIGHTS

A zinc-bromine static battery with regular sandwich-type configuration

Self-discharge was suppressed by converting soluble Br_2/Br_3^- species to solid phase

Zinc dendrite growth was inhibited by the adsorption of TPA^+ on the zinc anode

Gao et al., iScience *23*, 101348
August 21, 2020
https://doi.org/10.1016/j.isci.2020.101348

iScience

CellPress
OPEN ACCESS

Article

A High-Performance Aqueous Zinc-Bromine Static Battery

Lujie Gao,[1,2] Zhuxin Li,[1] Yiping Zou,[1] Shuangfeng Yin,[1] Peng Peng,[3] Yuying Shao,[3] and Xiao Liang[1,2,4,*]

SUMMARY

The highly reversible zinc-bromine redox couple has been successfully applied in the zinc-bromine flow batteries; however, non-electroactive pump/pipe/reservoir parts and ion-selective membranes are essential to suppress the bromine diffusion. This work demonstrates a zinc-bromine static (non-flow) battery without these auxiliary parts and utilizing glass fiber separator, which overcomes the high self-discharge rate and low energy efficiency while the advantages of the zinc-bromine chemistry are well preserved. It is achieved by a multifunctional additive, tetrapropylammonium bromide (TPABr), which not only mitigates the bromine cross-diffusion by regulating the fluidic bromine to a condensed solid phase but also provides a favorable interface for zinc electrodeposition toward non-dendritic growth. The proposed zinc-bromine static battery demonstrates a high specific energy of 142 Wh kg^{-1} with a high energy efficiency up to 94%. By optimizing the porous electrode architecture, the battery shows an ultra-stable cycling life for over 11,000 cycles with controlled self-discharge rate.

INTRODUCTION

Energy storage devices with high energy density, long cycling life, and low cost are eternal goals to meet the ever-increasing demands from portable electronic devices, electric vehicles, and renewable energy sources (Armand and Tarascon, 2008). Conventional lithium-ion batteries have dominated the market for decades owing to their relatively high energy density (150 Wh kg^{-1}) (Dunn et al., 2011; Nitta et al., 2015). However, the inherent safety hazard of the flammable organic electrolyte and high cost limit their large-scale applications such as for stationary energy storage (Tarascon and Armand, 2001; Turcheniuk et al., 2018). Flow batteries with multiple redox couples in aqueous media are one of the most promising technologies for large-scale energy storage (Yang et al., 2011). Among them, zinc-bromine flow batteries are very appealing, owing to their attractive features of long cycling life (Soloveichik, 2015).

A typical Zn-Br_2 flow battery is composed of two reservoirs for storage of the $ZnBr_2$ electrolyte, which are connected to the reactor by pumps/pipes (Ke et al., 2018). The basic redox reactions in the battery are summarized as following equations:

At the positive electrode:

$$2\ Br^- \leftrightarrow Br_2 + 2\ e^-\ (E^o = 1.08\ V\ versus\ SHE)$$

At the negative electrode:

$$Zn^{2+} + 2\ e^- \leftrightarrow Zn\ (E^o = -0.76\ V\ versus\ SHE)$$

Overall reaction:

$$Zn^{2+} + 2\ Br^- \leftrightarrow Br_2 + Zn\ (E^o = 1.84\ V)$$

During the charge process, Br_2 is generated at the positive electrode and further complexes with Br^- in aqueous media to form highly soluble Br_3^- ions, while zinc is deposited at the negative electrode simultaneously (Noack et al., 2015). Reverse reactions occur at the respective electrodes during the discharge process, providing a high theoretical energy density of 432 Wh kg^{-1} (Biswas et al., 2017; Darling et al., 2014).

[1]State Key Laboratory of Chem/Biosensing and Chemometrics, College of Chemistry and Chemical Engineering, Hunan University, Changsha 410082, P.R. China

[2]Advanced Catalytic Engineering Research Center of the Ministry of Education, Hunan University, Changsha 410082, P.R. China

[3]State Grid Shanghai Municipal Electric Power Company, 310 South of Chongqing Road, Shanghai 200025, P. R. China

[4]Lead Contact

*Correspondence: xliang@hnu.edu.cn

https://doi.org/10.1016/j.isci.2020.101348

Although the highly soluble Br_3^- species accelerates the redox kinetics, it reacts with the zinc anode directly by cross-diffusion, leading to self-discharge and low coulombic efficiency (Huskinson et al., 2014; Wang et al., 2017). Another existing issue for zinc-based battery is the dendritic Zn deposition, which potentially triggers an internal short circuit (Li et al., 2018a, 2018b; Yuan et al., 2018). These challenges are alleviated with the multiple approaches of a standard Zn-Br_2 flow battery: (1) Bromine complexing agents transform the soluble Br_3^- species to oily phase (Winsberg et al., 2017; Wu et al., 2019); (2) storage of the oily phase in separated reservoirs allows bromine convection and improves the limiting current density for Zn deposition (Gur, 2018; Soloveichik, 2015); (3) ion-selective membrane further prevents cross-diffusion and short circuits (Hu et al., 2017; Zhang et al., 2019). These approaches are compromised at the expense of cell resistance, energy efficiency (normally <80%), and increased system size and complexity (Biswas et al., 2017; Zhao et al., 2015). They sharply increase the capital costs from $8 per kWh based on $ZnBr_2$ electrolyte and carbon electrode to over $200 per kWh for a battery system, which is not superior at all when compared with the current Li-ion technology (Biswas et al., 2017; Winter et al., 2018). The flowable and corrosive Br_2/Br_3^- species further reduce the reliability of the system, leading to cell failure by parts corrosion instead of by the intrinsic redox chemistry (Evanko et al., 2018).

In typical Zn-Br_2 flow batteries, converting the soluble Br_2/Br_3^- species to oily complexation phase by asymmetric quaternary ammonium salts such as methyl ethyl pyrrolidinium bromide (MEPBr) or methyl ethyl morpholinium bromide (MEMBr) does not fully address the cross-diffusion and poor coulombic efficiency (Soloveichik, 2015; Xie et al., 2017). Auxiliary components such as microporous polyolefin or Daramic membrane and the bromine storage system (reservoirs, pumps, pipes) as discussed above are essential to achieve an acceptable performance (Huskinson et al., 2014; Park et al., 2017). Since most of these auxiliary components in Zn-Br_2 flow battery are correlated to address the cross-diffusion of the Br_2/Br_3^- species, the most straightforward strategy to simplify the battery system is transforming the soluble species to solid phase. In short, this requires a fundamental change to store Br_2/Br_3^- species in non-flow energy storage systems in a manner that suppresses cross-diffusion and self-discharge by a simple and affordable mechanism, as proposed by Stucky et al. for the aqueous redox-enhanced electrochemical capacitors (Yoo et al., 2017). Efforts had been made recently to realize flowless Zn-Br_2 batteries by entrapment of Br_3^- in the cathodes; however, the coulombic efficiencies are normally lower than 90% and the energy efficiencies are lower than 80% (Chun et al., 2015; Lee et al., 2019).

In this work, we demonstrate a zinc-bromine static (non-flow) battery without the auxiliary moving parts and utilizing a glass fiber separator, which overcomes the high self-discharge rate and low energy efficiency while the advantages of the zinc-bromine redox couple are well maintained. This is achieved by an effective complexing agent, tetrapropylammonium bromide (TPABr), reversibly converting the Br_2/Br_3^- species to solid phase in aqueous media. The solid complexation is stored in porous carbons with good interfacial contact, further providing physical confinements to prevent the cross-diffusion and self-discharge. We also witness the zinc electrodeposition is altered from dendritic to non-dendritic growth by the polar TPA^+ ions, which prefer to be adsorbed on zinc nucleus, blocking the strong electric field and regulating the ion distribution on the interface (Ding et al., 2013). In such a simplified design, the Zn-Br_2 static battery has a similar configuration to the Li-ion batteries. The proposed zinc-bromine static battery demonstrates a high specific energy density of 142 Wh kg^{-1} at 500 mA g^{-1} (equivalent to 150 W kg^{-1}) with a high energy efficiency of 94%. Note that the current densities and specific capacities are based on the mass of cathodes only, whereas the power densities and energy densities are calculated with the total mass of the cathode and active materials in electrolytes ($ZnBr_2$ and TPABr). Owing to the highly reversible bromine capture capacity of the TPABr additive, the battery shows an ultra-stable cycling life for over 11,000 cycles with minimum self-discharge rate. Our static battery configuration offers a cost-effective and easy fabrication path for spreading the Zn-Br_2 battery to practical application.

RESULTS

Reversible Solid Complexation of Br_2 in Aqueous Media

The non-flow zinc-bromine battery with regular porous glass fiber separator is particularly prone to low coulombic efficiency, as shown by the blank electrolyte (Figure 1A). This is due to the serious cross-diffusion of the highly soluble Br_2/Br_3^- species, which results in direct redox reaction with the zinc anode. Although the diffusion is alleviated in flow batteries by the combination of the ion-selective membranes and the bromine complexing agents (such as MEPBr), the zinc-bromine flow batteries are still plagued by self-discharge and low coulombic efficiency (Biswas et al., 2017). Relying solely on the MEPBr additive does

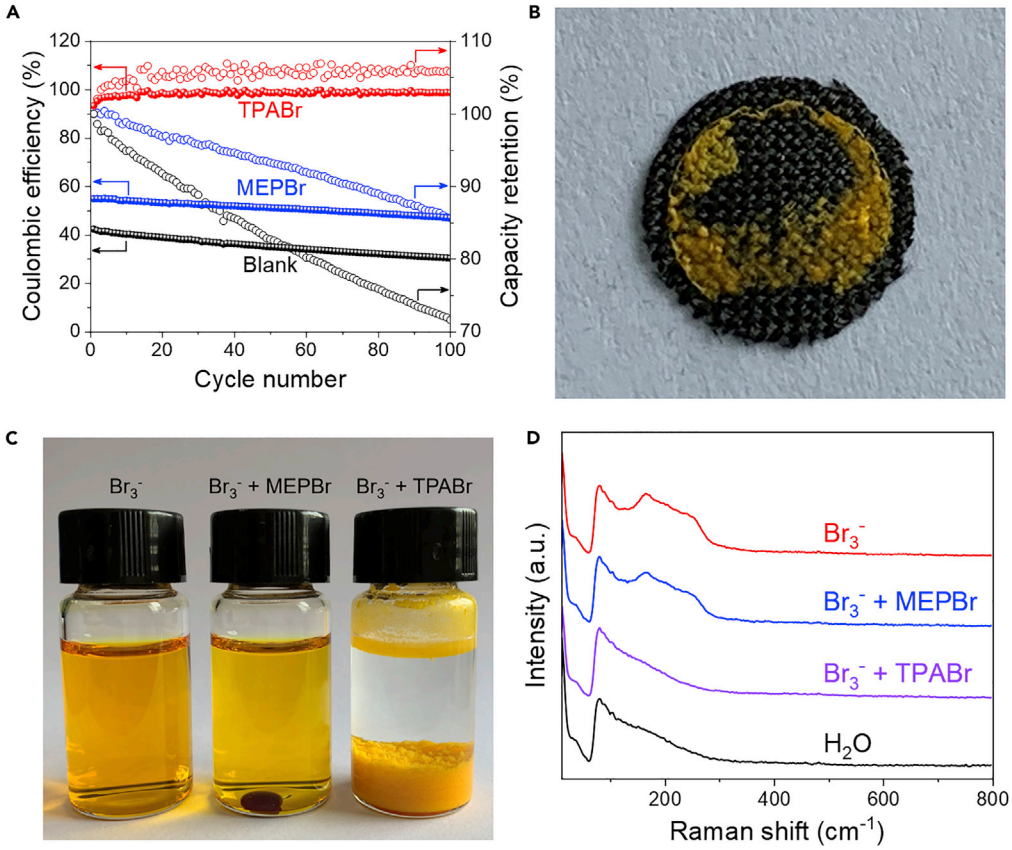

Figure 1. Properties of Bromine Complexing Agents

(A) Coulombic efficiencies and capacity retentions of the static batteries with (1) blank ($ZnBr_2$), (2) MEPBr, and (3) TPABr electrolytes at 100 mA g^{-1} (0.3 mA cm^{-2}).

(B) The image of the carbon cloth electrode after being charged for 1 h at 5 mA cm^{-2} in TPABr electrolyte.

(C) Br_3^- solution and its complexation by MEPBr and TPABr, respectively.

(D) Raman spectra of the Br_3^- solution and the supernatants of the Br_3^- + MEPBr and the Br_3^- + TPABr mixtures.

not show much improvement for coulombic efficiency in the static battery (Figure 1A). In sharp contrast, the static zinc-bromine battery with the TPABr complexing agent shows high reversibility with decent coulombic efficiency of 99.6%, as shown in Figure 1A. It is much higher than that of the recently reported "flowless" Zn-Br_2 batteries, which only show coulombic efficiencies of <90% (Lee et al., 2019). We ascribe it to the strong complexing ability of the TPABr additive, which fully transforms the soluble Br_2/Br_3^- species to solid phase in the electrode. Figure 1B shows the electrochemical generation of a solid complex on the surface of a carbon cloth electrode by passing anodic current in the $ZnBr_2$/TPABr electrolyte.

We studied the complexation chemistry of Br_3^- with TPABr and other quaternary ammonium salts with different chain length to demonstrate the effectiveness of suppressing the cross-diffusion (see Figure S1 for the molecular structure). Figure 1C and Figure S2 visually show the complexing product of the freshly prepared Br_3^- solution with quaternary ammonium salts (see Methods for detail). Conventional complexing agent of MEPBr for flow batteries is also shown for comparison. The yellow Br_3^- anion solution is immediately transferred into a colorless supernatant with solid precipitation by the TPABr additive, whereas MEPBr forms an oily liquid with certain amount of Br_3^- residual in the supernatant, as shown in Figure 1C. The supernatant was further characterized by Raman spectrum (Figure 1D). The symmetric stretching band of Br_3^- at 165 cm^{-1} is obvious in the MEPBr mixture (Chen et al., 2010; Yoo et al., 2017), implying insufficient complexation by MEPBr additive. The residual Br_3^- in the supernatant leads to cross-diffusion, which inevitably decreases the overall columbic efficiency, as shown in Figure 1A. However, the TPABr complexed supernatant is colorless with minor Raman response, verifying that no Br_3^- remains in the supernatant after

complexing. This is consistent with the high coulombic efficiency of the cell with the TPABr complexing agent. This approach is vastly different than the electrostatic attraction mechanism proposed to retain bromine species by the oppositely charged electrodes, which only shows a minor effect on the suppression of self-discharge (Chun et al., 2015). The precipitate discussed here is identical to the $TPABr_3$ solid complex formed electrochemically on the electrodes, as confirmed by Raman spectrum (Figure S3) and XRD pattern (Figure S4).

It is worth noting that the voltage profile of the cell with the TPABr electrolyte is significantly different from that of the MEPBr electrolyte, as shown in Figure 2A. Notably, the voltage of the cell with TPABr rises at the end of the charge process, followed by a "knee" point at the beginning of discharge. The large polarization of CMK-3 electrode at the beginning of the discharge is due to blocking of the pores of the electrode by the non-conductive $TPABr_3$ precipitation, which impedes the charge transfer path. Subsequent formation of $TPABr_3$ will aggregate on the electrode surface at the end of charge process, as shown by the SEM image of the charged carbon cloth electrode (Figure 2B). Figure S5 shows the corresponding SEM images of the CMK-3 electrode at different SOC; it is obvious that the surface of the electrode was covered by $TPABr_3$ crystals after it was fully charged (Figure S5F) but it disappeared after discharge (Figure S5G). It is understandable that the $MEPBr_3$ is a flowable oily phase that does not prefer to adsorb on the substrates so a flat voltage is obtained, as evidenced by the clean charged electrode (Figure S6). This phenomenon is supported by the electrochemical impedance spectroscopy (EIS) of the cell at different state of charge (SOC) (Figures 2C and 2D). The semicircles at the high frequency and middle frequency regions are corresponding to the ion migration process and the charge-transfer process, respectively (Orazem and Tribollet, 2017). Obviously, the charge-transfer impedance increases during the charge process with a sudden increase at the end of charge, which results in the rising of the charge potential simultaneously. The high charge transfer resistance is also attributed to the high polarization at the beginning of discharge. But it returns to a normal level with the consumption of the solid bromine phase on the electrode. In contrast, the impedance of the blank cell and MEPBr cell does not show such features (Figure S7).

Note that the cell has very stable cycling performance with a high coulombic efficiency of 99.6% even when a higher cutoff voltage of 2.2 V is applied (Figure S8). The high coulombic efficiency indicates that the plateau at 2.2 V is attributed to the electrodeposition of $TPABr_3$ on the electrode instead of water splitting. However, the large polarization at high cutoff voltage will definitely decrease the energy efficiency. So, the charge cutoff voltage is set only about 0.1 V higher than the charge voltage plateau. This highlights the importance of the porosity of the electrode to the specific capacity of the cell, which will be discussed in the next section. Figure S9 shows the cyclic voltammogram (CV) curves of the three cells. Different from the other two cells, the cathodic currents of the TPABr cell do not fluctuate with the change of scan rate. Although it is clear that the electrochemical process of the bromine chemistry in solution is controlled by diffusion process, the constant cathodic peak current of the cell with the TPABr additive indicates that the formation of the solid product determines the reaction rate.

Self-discharge is one of the most critical parameters for energy storage systems, determining the performance after intermittent application or storage (Palacin and de Guibert, 2016). Simply transferring the flow-type Zn-Br_2 battery to a non-flow battery without using microporous membrane represents a system with serious self-discharge, owing to the fast cross-diffusion of the soluble Br_2/Br_3^- species. We constructed transparent cells to demonstrate the mechanism of self-discharge (Figure S10). All cells were galvanostatically charged at 20 mA. It is obvious that the blank electrolyte and the MEPBr electrolyte changed to yellowish (color of the Br_2/Br_3^- species) only after 10 min of charge, implying a large amount of Br_3^- had diffused into electrolytes. It results in direct reaction between Br_3^- in the electrolytes and the zinc anode, namely, severe self-discharge. In sharp contrast, the TPABr electrolyte remained colorless after 2 h of charge with yellow precipitate on the electrode (Figure S10). We thus anticipate superior anti-self-discharge property with the TPABr additive because the formation of $TPABr_3$ solid complexes will greatly suppress the cross-diffusion. We quantified the self-discharge by testing the retained capacity after storage using a charged (activated) Zn-Br_2 cell at open-circuit voltage (OCV), as shown in Figure 2E. All cells were charged to the same specific capacity of 180 mAh g^{-1} (0.54 mAh cm^{-2}) at a current of 500 mA g^{-1} (1.5 mA cm^{-2}, 21.6 min). The OCV of each cell was recorded during the rest period. Not surprisingly, the blank cell demonstrates a very fast self-discharge rate. Its coulombic efficiency drops from 70% to 32% after only 1 h. Although MEPBr additive can partially complex the Br_3^- anion as an oily phase as discussed above, its coulombic efficiency still reduces by 30% after 1 h. Only about 20% of the capacity can be delivered after

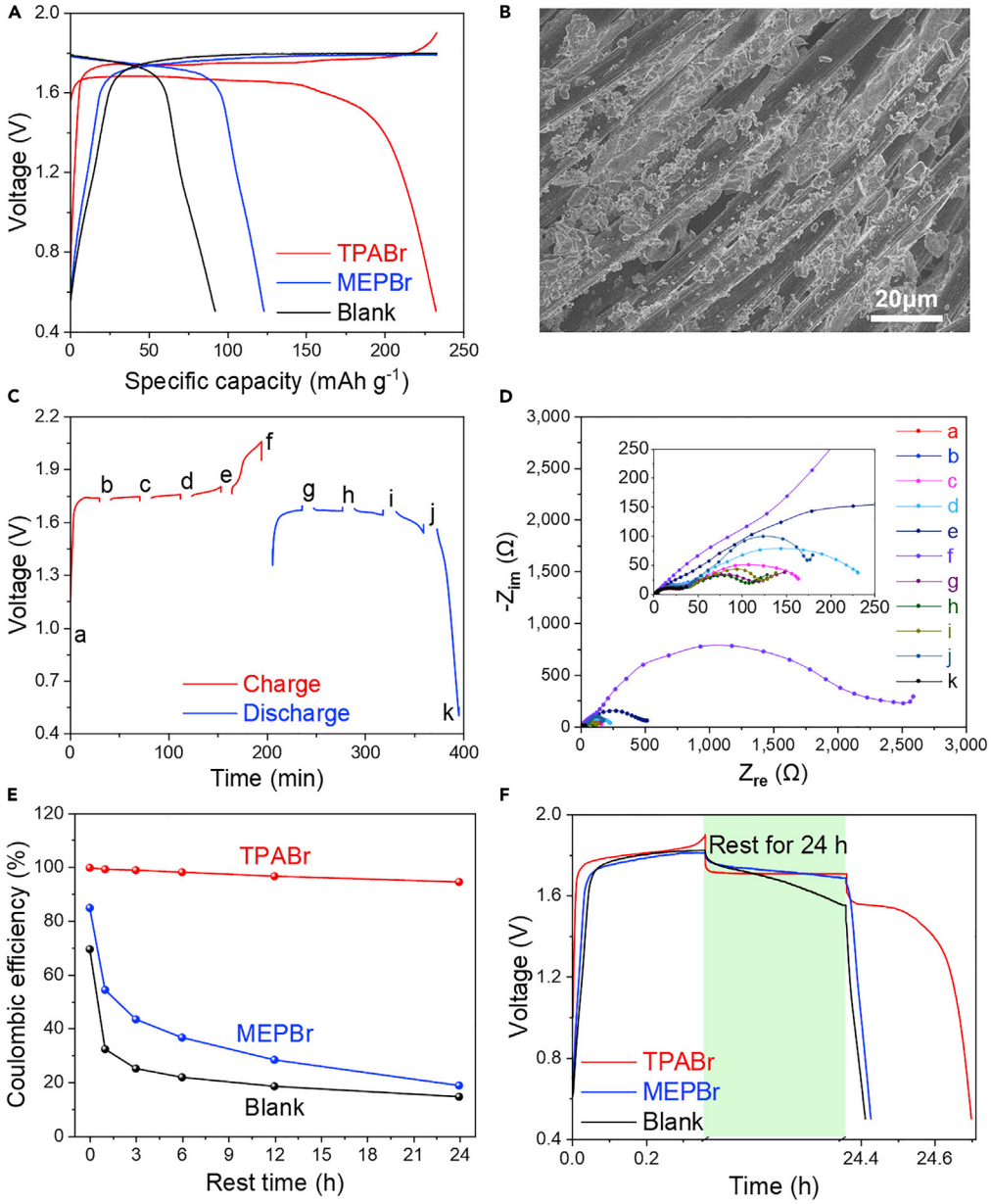

Figure 2. Electrochemical Behaviors of the Static Batteries with Different Electrolytes

(A) Voltage profiles at 100 mA g^{-1} (0.3 mA cm^{-2}).

(B) SEM image of the carbon cloth electrode after being charged for 1 h at 1 mA cm^{-2} in TPABr electrolyte.

(C and D) EIS spectra of the battery with TPABr at different SOC and the corresponding voltage profile at 100 mA g^{-1} (0.3 mA cm^{-2}).

(E) Coulombic efficiencies of the batteries versus rest time between charge and discharge processes at 500 mA g^{-1} (1.5 mA cm^{-2}).

(F) Voltage profiles with 24 h of rest between charge and discharge processes at 500 mA g^{-1} (1.5 mA cm^{-2}).

24 h of storage for these two cells, implying the fast redox with zinc anode caused by the Br_3^- anion cross-diffusion. On the contrary, the cell with the TPABr additive shows minor self-discharge after 1 h of rest. Remarkably, the coulombic efficiency only drops by 4% after 24 h of storage. Note that, even when utilizing a Nafion membrane with complicated system design, conventional zinc-bromine flow Battery still suffers a self-discharge rate of 10% per day (Lim et al., 1977; Yang et al., 2011). Figure 2F shows the voltage profiles with a rest period of 24 h. The OCV of the two control cells decayed continuously during the rest period,

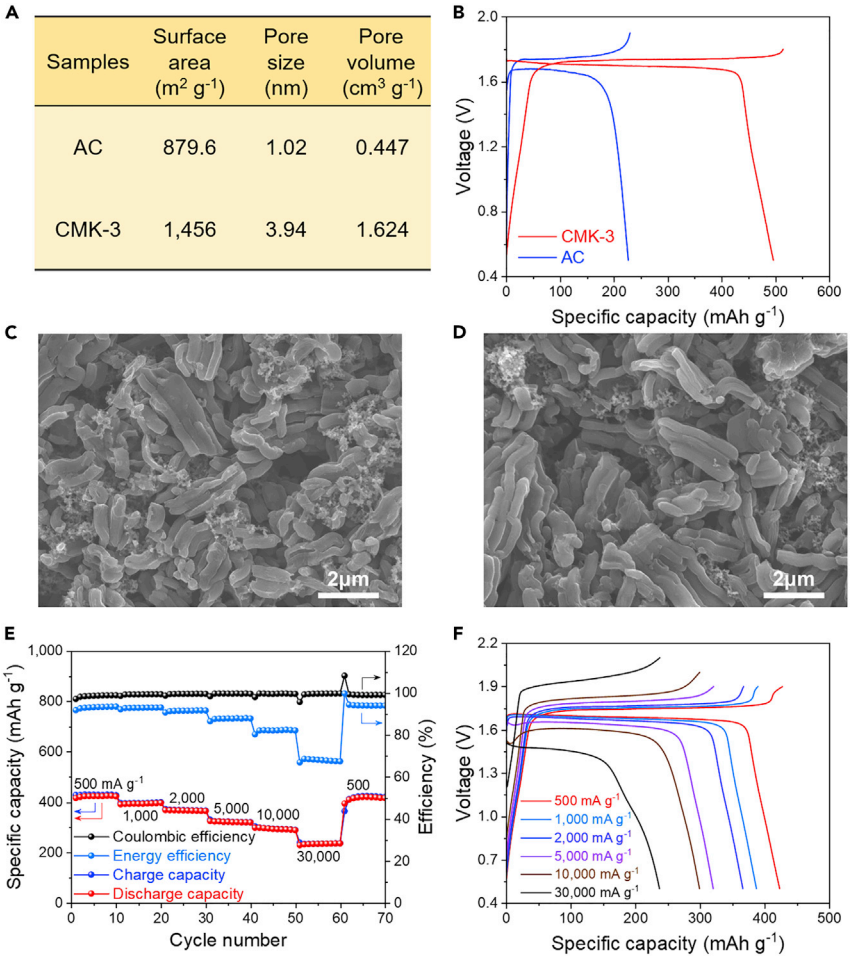

Figure 3. Rate Performances of the Zinc-Bromine Static Batteries with the TPABr Additive

(A) Comparison of the physical characteristics of activated carbon (AC) and CMK-3.

(B) Comparison of the charge and discharge voltage profiles of the batteries with activated carbon (AC) cathode and CMK-3 cathode at 100 mA g^{-1} (0.3 mA cm^{-2}).

(C) SEM image of the fresh CMK-3 electrode.

(D) SEM image of the fully charged CMK-3 electrode.

(E and F) Rate performance of the battery with CMK-3 cathode and the corresponding charge and discharge voltage profiles. Current densities and specific capacities are based on the mass of cathode.

leading to the disappearance of the following discharge voltage plateau. However, the cell with TPABr has a constant OCV, implying the cross-diffusion is greatly suppressed by the TPABr complexing agent.

Storing the Solid Br_2/Br_3^- Species in Porous Carbon

Although the mobility of Br_2/Br_3^- is successfully controlled by TPABr complexing agent, exploring a robust conductive porous material to contain the solid phase is essentially important for a static Zn-Br_2 battery. Obviously, similar to Li-S battery where pores provide physical confinement for the soluble polysulfides (Chen et al., 2019; Pang et al., 2016), a substrate with large surface area and pore volume is highly desired for the static Zn-Br_2 battery. We systematically compared two kinds of popular porous carbon substrates: activated carbon and CMK-3. Brunauer-Emmett-Teller (BET) analysis suggests that the activated carbon has a specific surface area of 879.6 m^2 g^{-1} and pore volume of 0.447 cm^3 g^{-1}, whereas the CMK-3 has a specific surface area of 1,456 m^2 g^{-1} and pore volume of 1.624 cm^3 g^{-1}, respectively (Figure 3A). Figure 3B shows the voltage profiles of the cells with these two electrodes, at a current density of 100 mA g^{-1} (0.3 mA cm^{-2}). The carbon loading of the electrodes is both about 3 mg cm^{-2}. Not surprisingly, the CMK-3 cathode delivers a much higher specific capacity than the activated carbon (497 versus 227 mAh g^{-1}, or 1.5 versus 0.7 mAh cm^{-2}). Figure S11 shows

the voltage profiles of the symmetric cell using $ZnCl_2$ solution as electrolyte and CMK-3 as both anode and cathode. It is a typical capacitor with the discharge specific capacity of about 43 mAh g^{-1} (0.1 mAh cm^{-2}), indicating the adsorbing of zinc ions only contributes a little capacity to the static battery. In contrast to the carbon cloth electrode with numerous $TPABr_3$ crystals on the surface (Figure 2B), the morphology of the fresh CMK-3 electrode and the fully charged CMK-3 electrode are identical (Figures 3C and 3D). Although the XRD patterns suggest there is a certain amount of $TPABr_3$ in the fully charged CMK-3 electrode (Figure S12), it indicates that the $TPABr_3$ is stored in the pores of CMK-3. BET analysis of the CMK-3 electrode recovered from the charged cell shows a vast decrease of pore volume (1.624 versus 0.025 cm^3 g^{-1}) (Figures S13B and S13C), again proving that the solid bromine phase is stored in the pores. This further indicates the significance of the pore volume in the performance of the Zn-Br_2 battery.

We witness a superior rate performance of the CMK-3 electrode (Figure 3E) than that of the activated carbon electrode (Figure S14A). The CMK-3 electrode delivers high specific capacities of 426, 398, 369, 326, and 300 mAh g^{-1} (1.3, 1.2, 1.1, 1.0, and 0.9 mAh cm^{-2}) at the current densities of 500, 1,000, 2,000, 5,000, and 10,000 mA g^{-1} (1.5, 3.0, 6.0, 15, and 30 mA cm^{-2}), respectively (Figure 3E). The corresponding energy efficiencies are 94%, 93%, 92%, 88%, and 83%, respectively. Remarkably, it delivers a specific capacity of 237 mAh g^{-1} (0.7 mAh cm^{-2}) with 70% energy efficiency at an ultrahigh current density of 30,000 mA g^{-1} (90 mA cm^{-2}, equivalent to 127 C). These performances are much better than that of the activated carbon (Figure S14A). The coulombic efficiency of the static Zn-Br_2 battery is likely to be independent of the current density, i.e., 99.5% coulombic efficiency is still achieved at slow current of 500 mA g^{-1} (1.5 mA cm^{-2}). This again implies that the Br_2/Br_3^- species are converted to solid phase and well stored in pores. The CMK-3 cell with MEPBr electrolyte only conveys very limited improvements over the cell with blank electrolyte, as shown in Figure S15. It is worth noting that the CMK-3 has a larger pore size than the activated carbon (3.94 versus 1.02 nm) (Figure 3A). We attribute the decent rate performance to the meso-sized pores of the CMK-3, which facilitate electrolyte penetration compared with micro-sized pores, particularly at high current densities. Figure 3F shows the corresponding voltage profiles of the CMK-3 electrode. Notably, the voltage plateaus are flatter than that of the activated carbon electrode (Figure S14B).

Inhibiting the Dendrite Growth

Dendrite growth is the main challenge for batteries with metal anodes (Li et al., 2018a, 2018b; Li and Dai, 2014). Although stable cycling performance of a practical battery relies on a favorable interface between the electrode and electrolyte, the dendritic feature of the zinc metal during plating gives rise to huge problem, particularly for long-term cycling (Wang et al., 2018). The zinc dendrite has a high surface area, which catalyzes the detrimental reaction with electrolyte. It also trends to detach from the anode, leading to fast capacity decay of the zinc-based batteries (Tan et al., 2017). The classic model suggests that the uneven distributions of electric field and zinc ion flow are the main factors for dendrite formation (Wang et al., 2015). During a typical electrodeposition process, zinc atoms nucleate at the active sites to form small protrusions, resulting in a stronger electric field and denser ion distribution above these areas (Parker et al., 2014). The following ions are more facile to deposit along these protrusions, which eventually aggregate as dendrite growth (Haxhimali et al., 2006). The Zn plating behavior in the TPABr electrolyte was revealed by SEM imaging. Zn electrodes were retrieved after plating 2 mAh cm^{-2} Zn at a current density of 5 mA cm^{-2} in Zn|Zn symmetric cells. The Zn plated in the blank electrolyte shows a typical needle-shaped morphology with large porosity (Figure 4A). The high-surface-area dendrites exacerbate reaction with the electrolyte, leading Zn pulverization after 100 h (125 cycles) of repeated plating/stripping (Figure 4D). In contrast, the Zn plated in the TPABr electrolyte shows more featureless with compact electrodeposition film (Figures 4C and 4F), implying non-dendritic zinc deposition. This is because the TPA^+ cation is a surfactant in nature and prefers to be absorbed on the zinc protrusions, which blocks the strong electric field and regulates the ion distribution on the interface (Ding et al., 2013). The Zn plated with the MEPBr additive has a similar condensed morphology, albeit forming islands instead of extensive film (Figure 4B). Nevertheless, these islands turn into big dendrites after 100 h (125 cycles) of repeated plating/stripping (Figure 4E). This is due to the higher surface activity and polarity of TPA^+ than that of MEP^+ (Nishiyama et al., 2005; Scott and Willett, 1991), enabling a more powerful absorbability. Repeat stripping/plating measurements were carried out in symmetric Zn|Zn cells to validate the long-term role of the TPABr additive. As shown in Figure 4G, the cell in the blank electrolyte only cycled for 26 h (33 cycles) before the cell failure by short circuit. In sharp contrast, the cell with TPABr additive showed a very stable potential profile for over 2,000 h (2,500 cycles) without any sign of a short circuit (Figure 4G, red). The over 70-fold improvement in cycling life proves that the additive is effective in stabilizing zinc electrodeposition. We further evaluated the

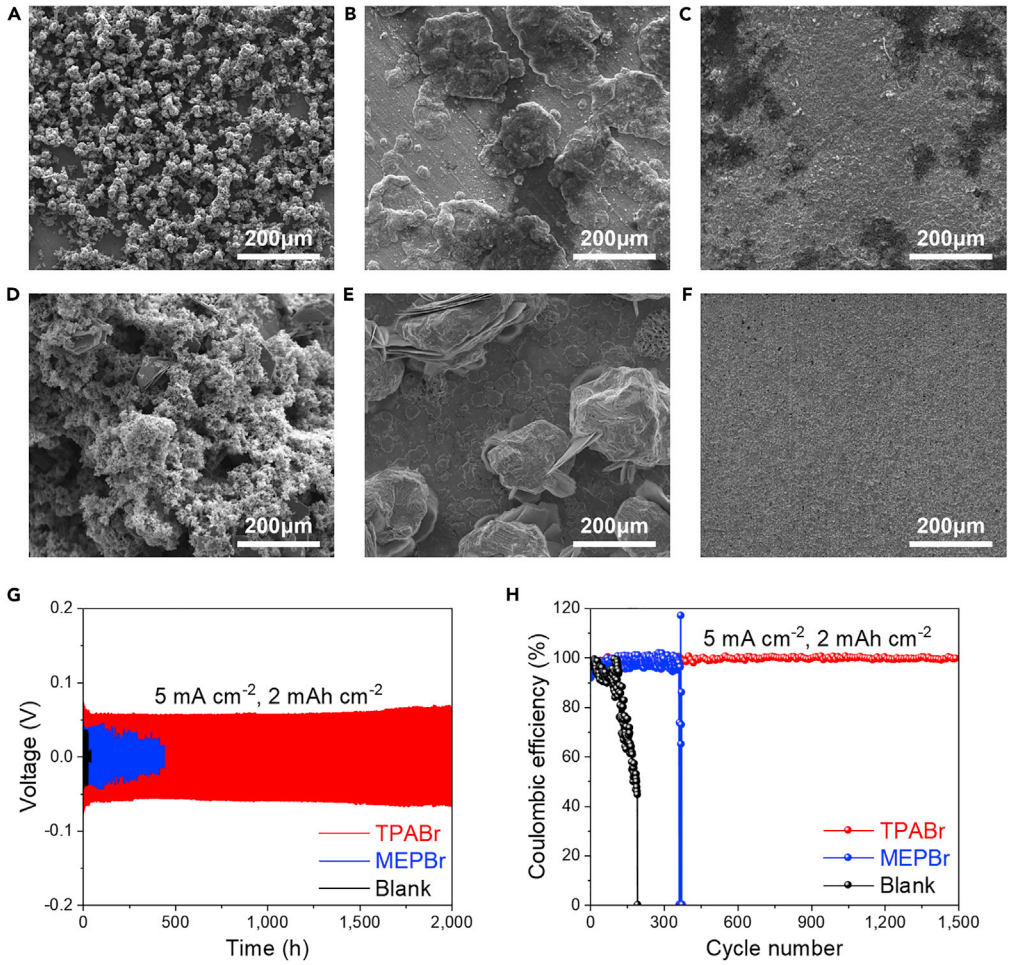

Figure 4. Zinc Platting/String Behaviors

(A–C) SEM images of the zinc anodes after once plating in (A) blank, (B) MEPBr, and (C) TPABr electrolytes, respectively.

(D–F) SEM images of the zinc anodes after stripping/plating for 100 h in (D) blank, (E) MEPBr, and (F) TPABr electrolytes, respectively.

(G) Voltage profiles of the Zn|Zn symmetric cells.

(H) Coulombic efficiencies of zinc stripping/plating on Cu foil.

stripping/plating reversibility in Zn|Cu cells to demonstrate the degree of the parasitic reaction (Tikekar et al., 2016) (Figure 4H). The coulombic efficiency of the cell in blank electrolyte demonstrated a drastic fluctuation and quickly decreased to 45% before a short circuit occurred at the 192th cycle. However, the cell with TPABr revealed a high coulombic efficiency at 99.9% and stable performance for over 1,500 cycles, demonstrating the favorable interface for Zn electrodeposition. As a result, not only the dendrite-related safety issue is resolved by the TPABr additive but also the electrolyte depletion is greatly suppressed, which avoids electrolyte drying out and will greatly extend the cycling life of the battery.

Long-Term Performance of the Zinc-Bromine Static Batteries

The complexing chemistry we explored that converts the Br_2/Br_3^- to solid phase is significantly different from the MEPBr agent for flow Zn-Br_2 battery and other approaches that bind Br_2/Br_3^- to the host by interactions (Lee et al., 2019). The soluble Br_2/Br_3^- species in electrolyte are remarkably precipitated as $TPABr_3$ solid complex, whereas free Br_2/Br_3^- is negligible. However, the MEPBr additive can only partially complex with Br_2/Br_3^- species as an oily liquid, which only shows little improvement over the static cell without a complexing agent. The $TPABr_3$ solid phase is stored in the meso-sized pores of CMK-3, guaranteeing charge transfer and further suppressing cross-diffusion in the cell. Moreover, electrodeposition of zinc is favorable with the TPABr additive, which solves the stability issue of the zinc anode. With all these improvements, we

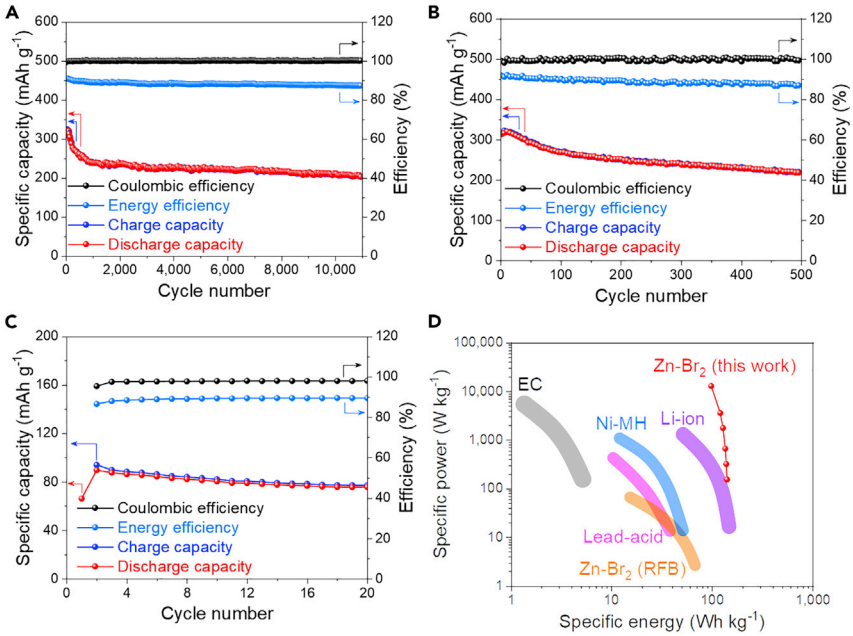

Figure 5. Electrochemical Performances of the Zinc-Bromine Static Batteries with the CMK-3 Electrode

(A) Long-term cycling stability at 5,000 mA g^{-1} (15 mA cm^{-2}).

(B) Cycling performance of the battery with Cu foil anode at 5,000 mA g^{-1} (15 mA cm^{-2}).

(C) Cycling performance of the battery with $TPABr_3$ cathode at 1.27 mA cm^{-2}.

(D) Comparison of the Ragone plot of the zinc-bromine static battery with several standard devices: electrochemical capacitors (EC), lead-acid batteries, nickel-metal hydride batteries, lithium-ion batteries, and zinc-bromine flow batteries. Data of these standard devices are cited from the literature (Lin et al., 2015; Shukla et al., 2001).

are allowed to study the long-term reversibility of the zinc-bromine redox couple in our simplified static cell. In such a device with exactly the same configuration as the Li-ion batteries, regular porous glass fiber is used as the separator without treatment.

Figure 5A shows the long-term cycling stability of the battery with CMK-3 electrode at 5,000 mA g^{-1} (15 mA cm^{-2}). The initial specific capacity is 324 mAh g^{-1} (1.0 mAh cm^{-2}), which decreases to 240 mAh g^{-1} (0.7 mAh cm^{-2}) after 1,000 cycles and 205 mAh g^{-1} (0.6 mAh cm^{-2}) after 11,000 cycles. The capacity degradation rate is 0.026% per cycle at the first 1,000 cycles, and for the remaining 10,000 cycles it is as low as 0.001% per cycle. The battery demonstrates a high coulombic efficiency of 99.9% and energy efficiencies of 87%–92%, respectively. We notice the energy efficiency increases with the decrease of the current density, as shown in Figure S16. The cell at 500 mA g^{-1} (1.5 mA cm^{-2}) current density has an energy efficiency of 94%, which is superior to that of the $Zn\text{-}Br_2$ flow battery and is comparable with the Li-ion technology (Biswas et al., 2017; Nitta et al., 2015).

Benefiting from the high stripping/plating efficiency of zinc in the electrolyte with TPABr additive, the static battery we proposed can even cycle stably without a zinc anode. A piece of Cu foil was used for Zn electrodeposition in a full battery. The discharge cutoff voltage was set at 1.1 V to avoid the plating/stripping of Cu. Remarkably, the battery delivers a comparably high initial specific capacity of 322 mAh g^{-1} (1.0 mAh cm^{-2}). A specific capacity of 218 mAh g^{-1} (0.7 mAh cm^{-2}) is maintained after 500 cycles with a high coulombic efficiency of 99.5% and energy efficiencies of 87%–92% (Figure 5B). The corresponding charge and discharge voltage profiles are shown in the Figure S17.

The aqueous zinc-bromine static battery represents a safe battery technology that could bear extensive destruction, such as cutting with scissors. There is no fire ignition or smoking during the destruction; instead, the output voltage is well maintained, as visually demonstrated by the Video S1.

We note the solubility of the electrolyte and the amount of electrolyte would affect the practical energy density. However, we here prove that using $TPABr_3$ as the active material in the cathode (the complexed

Battery Type	Maximum Energy Density (Wh kg^{-1})	Maximum Power Density (W kg^{-1})	Coulombic Efficiency (%)	Energy Efficiency (%)	Cycling Life	Reference
Zn-Br_2 (flow)	135	NA	95	75	1,000	(Biswas et al., 2017)
Zn-Br_2 (single)	NA	NA	92	82	70	(Lai et al., 2013)
Zn-Br_2 (supercapattery)	90	3,100	99	NA	7,000	(Yu et al., 2020)
EV-Br_2 hybrid supercapacitor	64	3,000	97	84	7,000	(Yoo et al., 2017)
AQDS-Br_2 flow battery	50	NA	95	NA	15	(Huskinson et al., 2014)
Zn-Br_2 (static)	142	13,000	99.9	94	11,000	This work

Table 1. Comparison of Different Energy Storage Devices Involving Zn-Br_2 Redox Couple or Based on Bromine Chemistry
For comparison, all energy densities were converted using the total weight of the positive, negative electrodes and the active material mass.

solid form of bromine during charge) could potentially solve the solubility dependency issue of the TPABr + $ZnBr_2$ electrolyte. As shown in Figure 5C, the battery demonstrates a high specific capacity of 90 mAh g^{-1}, or 6.3 mAh cm^{-2}, based on the total mass of the cathode (weight of $TPABr_3$, CMK-3, super P, and PVDF), together with a high coulombic efficiency of 99.5% and energy efficiency of 90% at a current density of 1.27 mA/cm^2. It is worth noting that the areal capacity of this battery is superior to state-of-the-art lithium ion batteries (6.3 versus 4 mAh cm^{-2}) and is much higher than the capacity delivered by the TPABr + $ZnBr_2$ electrolyte (2.7 mAh cm^{-2}).

The Ragone plot in Figure 5D shows the comparison of the zinc-bromine static battery with several other standard devices (Lin et al., 2015; Shukla et al., 2001). The power density and energy density of the zinc-bromine static battery is based on the total mass of the cathode (CMK-3, super P, and PVDF) and the active materials in electrolyte ($ZnBr_2$ and TPABr). The zinc-bromine static battery delivers a high energy density of 142 Wh kg^{-1} at a power density of 150 W kg^{-1}. Impressively, even at an ultrahigh power density of 13 kW kg^{-1} (exceeding the maximum power density of electrochemical capacitors), it still retains a high energy density of 99 Wh kg^{-1}. The power performance is much superior to other zinc-based batteries involving metal oxide intercalation electrodes (Kundu et al., 2016; Pan et al., 2016). Table 1 summarizes the key parameters of the energy storage devices involving Zn-Br_2 redox couple or based on bromine chemistry (Biswas et al., 2017; Huskinson et al., 2014; Lai et al., 2013; Yoo et al., 2017; Yu et al., 2020). These batteries, mainly run with the "flowing electrolyte" concept and are plugged with high cell polarization and complicated system design. They are challenged by the low energy efficiencies and high capital costs, which are key parameters for large-scale energy storage. In contrast, the zinc-bromine static battery delivers a higher energy density, power density, energy efficiency, and longer cycling life. Overall, these results demonstrate that the zinc-bromine redox couple in a simple cell configuration as the Li-ion batteries can deliver stable long-term cycling performance with high energy as well as power densities.

DISCUSSION

The zinc-bromine chemistry is promising for large-scale energy storage, as demonstrated by the commercialized Zn-Br_2 flow battery in the past decades. However, the complicated system and the resulted high capital costs of the Zn-Br_2 flow battery made it not superior to the current Li-ion technology. We proposed a revolutionary battery configuration to demonstrate the advantages of the zinc-bromine redox couple. In such a simplified module, all the auxiliary components such as the microporous polyolefin or Daramic membrane and the electrolyte flowing system for flow batteries are eliminated. Instead, the Zn-Br_2 static battery has a regular sandwich-type configuration with the readily available glass fiber as the separator, which is as simple as a typical Li-ion battery. This is enabled by regulating the active Br_2/Br_3^- species in the battery from a highly soluble phase to solid phase by a multifunctional additive. The TPABr additive in electrolyte converts the soluble Br_2/Br_3^- species by reversible complexation. By the combination with a highly porous CMK-3 electrode, the cross-diffusion and self-discharge are fundamentally resolved. The aforementioned auxiliary components are thus excluded while all the advantages of the Zn-Br_2 redox couple are well

maintained. Although the long-term cycling of the zinc metal-based batteries is challenged by the dendritic growth on Zinc anode, it is simultaneously overcome by the multifunctional TPABr additive, which shows favorable interface for zinc electrodeposition toward non-dendrite growth. The Zn-Br_2 static battery we proposed demonstrates a high specific energy of 142 Wh kg^{-1} at 500 mA g^{-1} (equivalent to 150 W kg^{-1}) with a high energy efficiency of 94%. In particular, the battery shows an ultra-stable cycling life for over 11,000 cycles with minimum self-discharge rate.

Given the fact that all materials in the battery are readily available and inexpensive, the static battery is anticipated to have a dramatic cutoff of the capital costs compared with the flow batteries. Moreover, the Zn-Br_2 static battery has a similar configuration as the Li-ion batteries but all of the components are not sensitive to moisture and oxygen. Dry rooms or other special environments are not required during cell assembly, further simplifying the scale-up production. Our static battery configuration offers a cost-effective, easy fabrication path for spreading the Zn-Br_2 battery to practical application.

Limitations of the Study

The zinc-bromine static battery we proposed here still suffers from little rate of self-discharge (4% per 24 h), which reflects the conversion of the soluble Br_2/Br_3^- species to the solid $TPABr_3$ phase is not complete. Further in-depth study about the complexing chemistry and its kinetics might afford a more efficient bromine complexing agent. In addition, the performance of the static cells was studied by using Swagelok cells instead of pouch cells. Thus, design of a pouch cell with Ah capacity is essential to evaluate the practical potential of this technology.

Resource Availability

Lead Contact

Further information and requests for resources and reagents should be directed to and will be fulfilled by the Lead Contact, Xiao Liang (xliang@hnu.edu.cn).

Materials Availability

This study did not generate new unique reagents.

Data and Code Availability

This study did not generate/analyze datasets/code.

METHODS

All methods can be found in the accompanying Transparent Methods supplemental file.

SUPPLEMENTAL INFORMATION

Supplemental Information can be found online at https://doi.org/10.1016/j.isci.2020.101348.

ACKNOWLEDGMENTS

We thank the financial support provided by National Key Research and Development Program, China (No. 2019YFA0210600), the State Grid Shanghai Municipal Electric Power Company (No. 520970190004), and the Innovative Research Groups of Hunan Province (No. 2019JJ10001).

AUTHOR CONTRIBUTIONS

L.G. and X.L. designed this study. L.G. prepared the materials and carried out the electrochemical experiments. L.G. conducted the Raman analyses and SEM studies. Z.L. conducted the XRD measurements. Y.Z. conducted the BET analyses. L.G. carried out data processing and prepared the figures. L.G. and X.L. wrote the manuscript. All authors contributed to the scientific discussion.

DECLARATION OF INTERESTS

The authors declare no competing interests.

Received: September 4, 2019
Revised: June 10, 2020
Accepted: July 3, 2020
Published: August 21, 2020

REFERENCES

Armand, M., and Tarascon, J.M. (2008). Building better batteries. Nature *451*, 652–657.

Biswas, S., Senju, A., Mohr, R., Hodson, T., Karthikeyan, N., Knehr, K.W., Hsieh, A.G., Yang, X.F., Koel, B.E., and Steingart, D.A. (2017). Minimal architecture zinc-bromine battery for low cost electrochemical energy storage. Energy Environ. Sci. *10*, 114–120.

Chen, X., Hou, T.Z., Persson, K.A., and Zhang, Q. (2019). Combining theory and experiment in lithium-sulfur batteries: current progress and future perspectives. Mater. Today *22*, 142–158.

Chen, X., Rickard, M.A., Hull, J.W., Jr., Zheng, C., Leugers, A., and Simoncic, P. (2010). Raman spectroscopic investigation of tetraethylammonium polybromides. Inorg. Chem. *49*, 8684–8689.

Chun, S.E., Evanko, B., Wang, X.F., Vonlanthen, D., Ji, X.L., Stucky, G.D., and Boettcher, S.W. (2015). Design of aqueous redox-enhanced electrochemical capacitors with high specific energies and slow self-discharge. Nat. Commun. *6*, 7818.

Darling, R.M., Gallagher, K.G., Kowalski, J.A., Ha, S., and Brushett, F.R. (2014). Pathways to low-cost electrochemical energy storage: a comparison of aqueous and nonaqueous flow batteries. Energy Environ. Sci. *7*, 3459–3477.

Ding, F., Xu, W., Graff, G.L., Zhang, J., Sushko, M.L., Chen, X.L., Shao, Y.Y., Engelhard, M.H., Nie, Z.M., Xiao, J., et al. (2013). Dendrite-free lithium deposition via self-healing electrostatic shield mechanism. J. Am. Chem. Soc. *135*, 4450–4456.

Dunn, B., Kamath, H., and Tarascon, J.M. (2011). Electrical energy storage for the grid: a battery of choices. Science *334*, 928–935.

Evanko, B., Yoo, S.J., Lipton, J., Chun, S.E., Moskovits, M., Ji, X.L., Boettcher, S.W., and Stucky, G.D. (2018). Stackable bipolar pouch cells with corrosion-resistant current collectors enable high-power aqueous electrochemical energy storage. Energy Environ. Sci. *11*, 2865–2875.

Gur, T.M. (2018). Review of electrical energy storage technologies, materials and systems: challenges and prospects for large-scale grid storage. Energy Environ. Sci. *11*, 2696–2767.

Haxhimali, T., Karma, A., Gonzales, F., and Rappaz, M. (2006). Orientation selection in dendritic evolution. Nat. Mater. *5*, 660–664.

Hu, B., DeBruler, C., Rhodes, Z., and Liu, T.L. (2017). Long-cycling aqueous organic redox flow battery (AORFB) toward sustainable and safe energy storage. J. Am. Chem. Soc. *139*, 1207–1214.

Huskinson, B., Marshak, M.P., Suh, C., Er, S., Gerhardt, M.R., Galvin, C.J., Chen, X.D., Aspuru-Guzik, A., Gordon, R.G., and Aziz, M.J. (2014). A metal-free organic-inorganic aqueous flow battery. Nature *505*, 195.

Ke, X.Y., Prahl, J.M., Alexander, J.I.D., Wainright, J.S., Zawodzinski, T.A., and Savinell, R.F. (2018). Rechargeable redox flow batteries: flow fields, stacks and design considerations. Chem. Soc. Rev. *47*, 8721–8743.

Kundu, D., Adams, B.D., Duffort, V., Vajargah, S.H., and Nazar, L.F. (2016). A high-capacity and long-life aqueous rechargeable zinc battery using a metal oxide intercalation cathode. Nat. Energy *1*, 8.

Lai, Q.Z., Zhang, H.M., Li, X.F., Zhang, L.Q., and Cheng, Y.H. (2013). A novel single flow zinc-bromine battery with improved energy density. J. Power Sources *235*, 1–4.

Lee, J.H., Byun, Y., Jeong, G.H., Choi, C., Kwen, J., Kim, R., Kim, I.H., Kim, S.O., and Kim, H.T.((2019). High-energy efficiency membraneless flowless Zn-Br battery: utilizing the electrochemical-chemical growth of polybromides. Adv. Mater. *31*, 1904524.

Li, G.X., Liu, Z., Huang, Q.Q., Gao, Y., Regula, M., Wang, D.W., Chen, L.Q., and Wang, D.H. (2018a). Stable metal battery anodes enabled by polyethylenimine sponge hosts by way of electrokinetic effects. Nat. Energy *3*, 1076–1083.

Li, L., Basu, S., Wang, Y.P., Chen, Z.Z., Hundekar, P., Wang, B.W., Shi, J., Shi, Y.F., Narayanan, S., and Koratkar, N. (2018b). Self-heating-induced healing of lithium dendrites. Science *359*, 1513–1516.

Li, Y.G., and Dai, H.J. (2014). Recent advances in zinc-air batteries. Chem. Soc. Rev. *43*, 5257–5275.

Lim, H., Lackner, A., and Knechtli, R. (1977). Zinc-bromine secondary battery. J. Electrochem. Soc. *124*, 1154–1157.

Lin, T.Q., Chen, I.W., Liu, F.X., Yang, C.Y., Bi, H., Xu, F.F., and Huang, F.Q. (2015). Nitrogen-doped mesoporous carbon of extraordinary capacitance for electrochemical energy storage. Science *350*, 1508–1513.

Nishiyama, N., Zheng, T., Yamane, Y., Egashira, Y., and Ueyama, K. (2005). Microporous carbons prepared from cationic surfactant-resorcinol/formaldehyde composites. Carbon *43*, 269–274.

Nitta, N., Wu, F.X., Lee, J.T., and Yushin, G. (2015). Li-ion battery materials: present and future. Mater. Today *18*, 252–264.

Noack, J., Roznyatovskaya, N., Herr, T., and Fischer, P. (2015). The chemistry of redox-flow batteries. Angew. Chem. Int. Ed. *54*, 9775–9808.

Orazem, M.E., and Tribollet, B. (2017). Electrochemical Impedance Spectroscopy (John Wiley & Sons).

Palacin, M.R., and de Guibert, A. (2016). Why do batteries fail? Science *351*, 7.

Pan, H.L., Shao, Y.Y., Yan, P.F., Cheng, Y.W., Han, K.S., Nie, Z.M., Wang, C.M., Yang, J.H., Li, X.L., Bhattacharya, P., et al. (2016). Reversible aqueous zinc/manganese oxide energy storage from conversion reactions. Nat. Energy *1*, 7.

Pang, Q., Liang, X., Kwok, C.Y., and Nazar, L.F. (2016). Advances in lithium-sulfur batteries based on multifunctional cathodes and electrolytes. Nat. Energy *1*, 11.

Park, M., Ryu, J., Wang, W., and Cho, J. (2017). Material design and engineering of next-generation flow-battery technologies. Nat. Rev. Mater. *2*, 18.

Parker, J.F., Chervin, C.N., Nelson, E.S., Rolison, D.R., and Long, J.W. (2014). Wiring zinc in three dimensions re-writes battery performance-dendrite-free cycling. Energy Environ. Sci. *7*, 1117–1124.

Scott, B., and Willett, R.D. (1991). A copper(II) bromide dimer system exhibiting piezochromic and thermochromic properties: the crystal structure and electronic spectroscopy of the two room-temperature phases of bis(tetrapropylammonium) hexabromodicuprate(II). J. Am. Chem. Soc. *113*, 5253–5258.

Shukla, A.K., Arico, A.S., and Antonucci, V. (2001). An appraisal of electric automobile power sources. Renew. Sust. Energ. Rev. *5*, 137–155.

Soloveichik, G.L. (2015). Flow batteries: current status and trends. Chem. Rev. *115*, 11533–11558.

Tan, P., Chen, B., Xu, H.R., Zhang, H.C., Cai, W.Z., Ni, M., Liu, M.L., and Shao, Z.P. (2017). Flexible Zn- and Li-air batteries: recent advances, challenges, and future perspectives. Energy Environ. Sci. *10*, 2056–2080.

Tarascon, J.M., and Armand, M. (2001). Issues and challenges facing rechargeable lithium batteries. Nature *414*, 359–367.

Tikekar, M.D., Choudhury, S., Tu, Z.Y., and Archer, L.A. (2016). Design principles for electrolytes and interfaces for stable lithium-metal batteries. Nat. Energy *1*, 1–7.

Turcheniuk, K., Bondarev, D., Singhal, V., and Yushin, G. (2018). Ten years left to redesign lithium-ion batteries. Nature *559*, 467–470.

Wang, C.H., Lai, Q.Z., Xu, P.C., Zheng, D.Y., Li, X.F., and Zhang, H.M. (2017). Cage-like porous carbon with superhigh activity and Br-2-complex-entrapping capability for bromine-based flow batteries. Adv. Mater. *29*, 6.

Wang, F., Borodin, O., Gao, T., Fan, X.L., Sun, W., Han, F.D., Faraone, A., Dura, J.A., Xu, K., and

Wang, C.S. (2018). Highly reversible zinc metal anode for aqueous batteries. Nat. Mater. *17*, 543.

Wang, K.L., Pei, P.C., Ma, Z., Chen, H.C., Xu, H.C., Chen, D.F., and Wang, X.Z. (2015). Dendrite growth in the recharging process of zinc-air batteries. J. Mater. Chem. A *3*, 22648–22655.

Winsberg, J., Hagemann, T., Janoschka, T., Hager, M.D., and Schubert, U.S. (2017). Redox-flow batteries: from metals to organic redox-active materials. Angew. Chem. Int. Ed. *56*, 686–711.

Winter, M., Barnett, B., and Xu, K. (2018). Before Li ion batteries. Chem. Rev. *118*, 11433–11456.

Wu, Y.T., Huang, P.W., Howe, J.D., Yan, Y., Martinez, J., Marianchuk, A., Zhang, Y.M., Chen, H., and Liu, N. (2019). In operando visualization of the electrochemical formation of liquid polybromide microdroplets. Angew. Chem. Int. Ed. *58*, 15228–15234.

Xie, C.X., Duan, Y.Q., Xu, W.B., Zhang, H.M., and Li, X.F. (2017). A low-cost neutral zinc-iron flow battery with high energy density for stationary energy storage. Angew. Chem. Int. Ed. *56*, 14953–14957.

Yang, Z.G., Zhang, J.L., Kintner-Meyer, M.C.W., Lu, X.C., Choi, D.W., Lemmon, J.P., and Liu, J. (2011). Electrochemical energy storage for green grid. Chem. Rev. *111*, 3577–3613.

Yoo, S.J., Evanko, B., Wang, X., Romelczyk, M., Taylor, A., Ji, X., Boettcher, S.W., and Stucky, G.D. (2017). Fundamentally addressing bromine storage through reversible solid-state confinement in porous carbon electrodes: design of a high-performance dual-redox electrochemical capacitor. J. Am. Chem. Soc. *139*, 9985–9993.

Yu, F., Zhang, C., Wang, F., Gu, Y., Zhang, P., Waclawik, E., Du, A., Ostrikov, K., and Wang, H. (2020). A zinc bromine "supercapattery" system combining triple functions of capacitive, pseudocapacitive and battery-type charge storage. Mater. Horiz. *7*, 495–503.

Yuan, Z.Z., Liu, X.Q., Xu, W.B., Duan, Y.Q., Zhang, H.M., and Li, X.F. (2018). Negatively charged nanoporous membrane for a dendrite-free alkaline zinc-based flow battery with long cycle life. Nat. Commun. *9*, 11.

Zhang, J.Y., Chen, J.X., Peng, S., Peng, S.Y., Zhang, Z.Z., Tong, Y.X., Miller, P.W., and Yan, X.P. (2019). Emerging porous materials in confined spaces: from chromatographic applications to flow chemistry. Chem. Soc. Rev. *48*, 2566–2595.

Zhao, Y., Ding, Y., Li, Y.T., Peng, L.L., Byon, H.R., Goodenough, J.B., and Yu, G.H. (2015). A chemistry and material perspective on lithium redox flow batteries towards high-density electrical energy storage. Chem. Soc. Rev. *44*, 7968–7996.

iScience, Volume *23*

Supplemental Information

A High-Performance Aqueous Zinc-Bromine Static Battery

Lujie Gao, Zhuxin Li, Yiping Zou, Shuangfeng Yin, Peng Peng, Yuying Shao, and Xiao Liang

Supplemental Figures

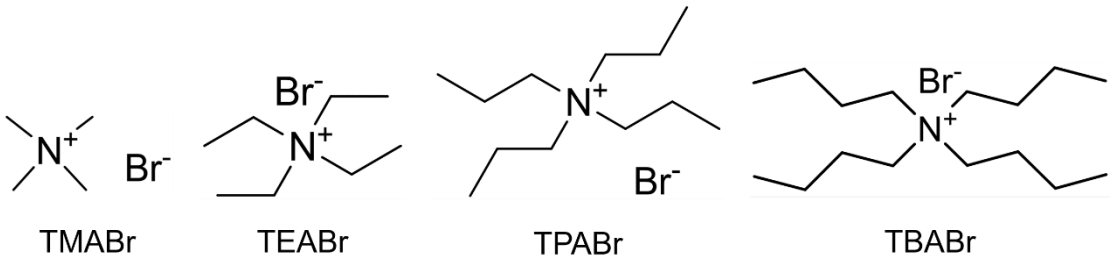

Figure S1. The structural formula of TPABr, related to Figure 1.

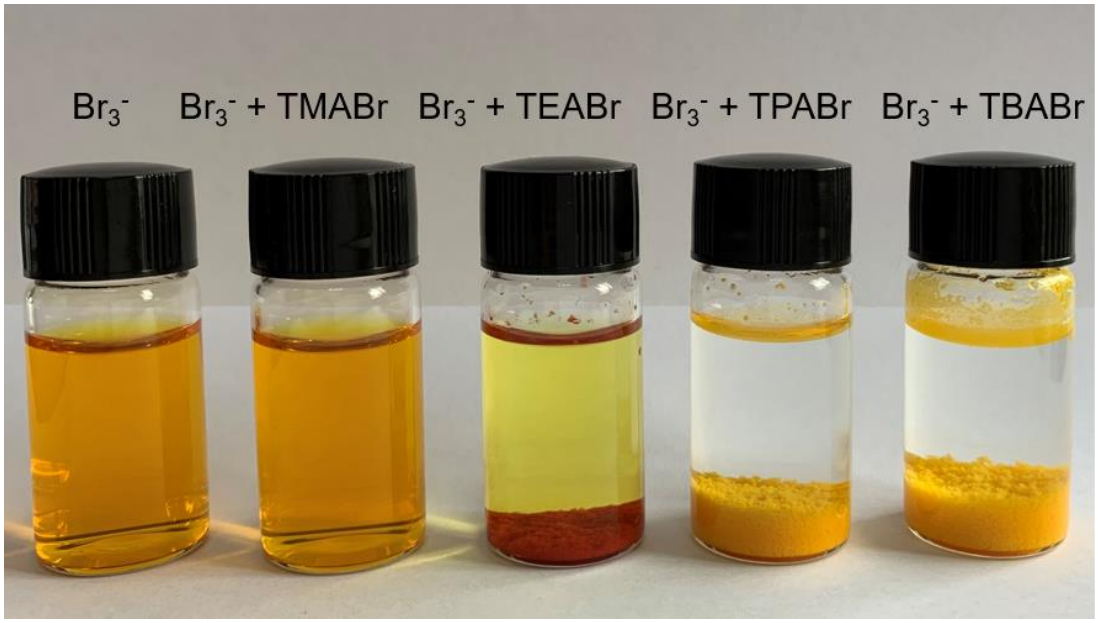

Figure S2. Br_3^- solution and its complexations by TMABr, TEABr, TPABr and TBABr, respectively, related to Figure 1.

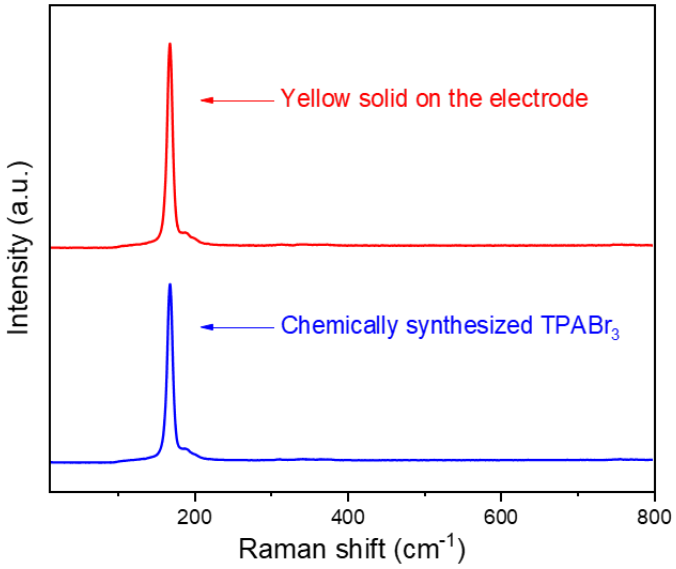

Figure S3. Raman spectra, related to Figure 1.

Raman spectra of the yellow solid generated in the charge process in the battery and the chemically synthesized $TPABr_3$.

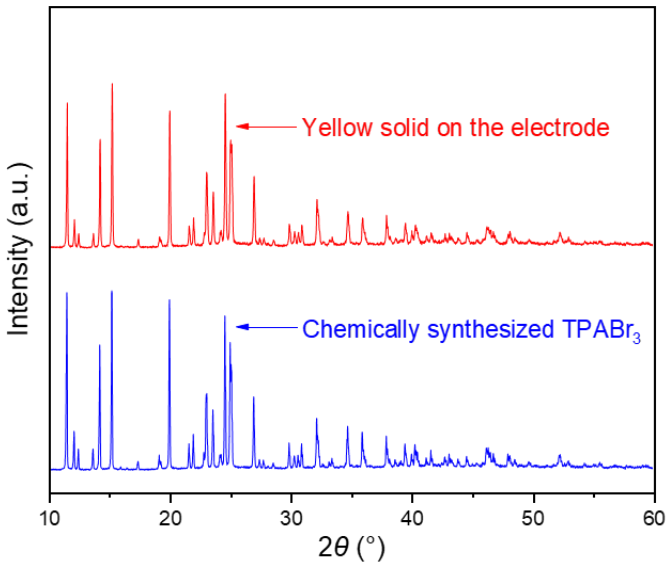

Figure S4. XRD patterns, related to Figure 1.

XRD patterns of the yellow solid generated in the charge process in the battery and the chemically synthesized $TPABr_3$.

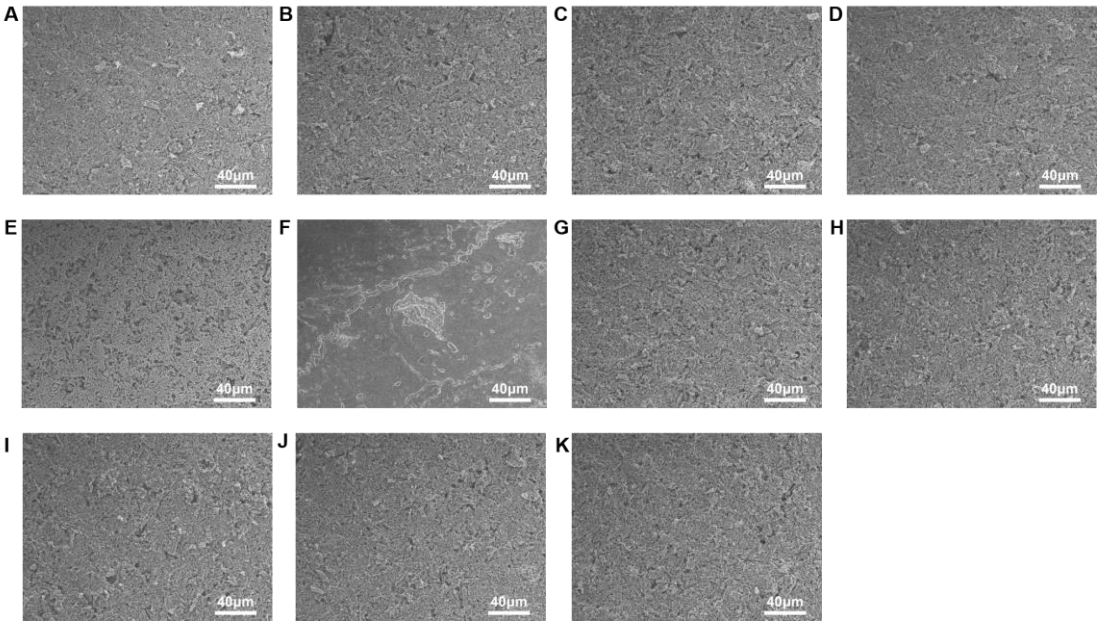

Figure S5. SEM images of the CMK-3 electrode at different SOC, related to Figure 3.

The letter numbers of the images are corresponded to the letter numbers in Figure S15C.

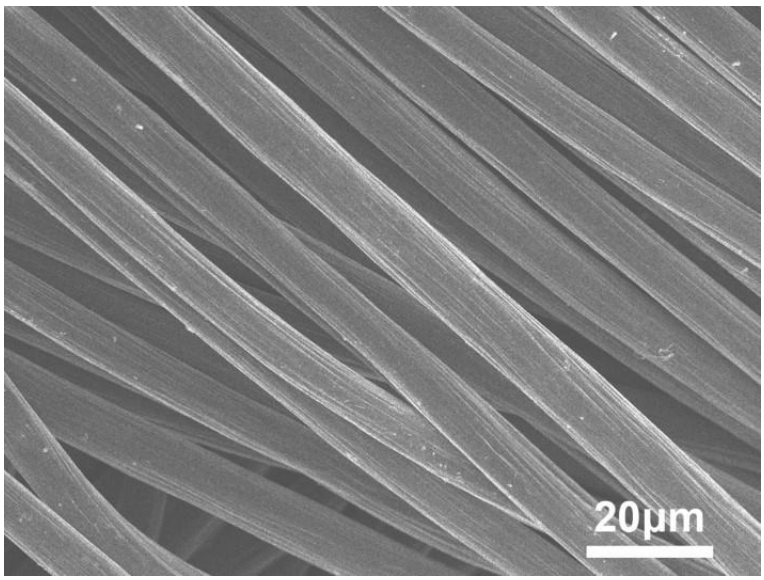

Figure S6. SEM image, related to Figure 2.

SEM image of the carbon cloth electrode after being charged for 1 hour at 1 mA cm^{-2} in MEPBr electrolyte. Clean surface indicates the oily Bromine complexing product is not absorbed on the carbon fibers.

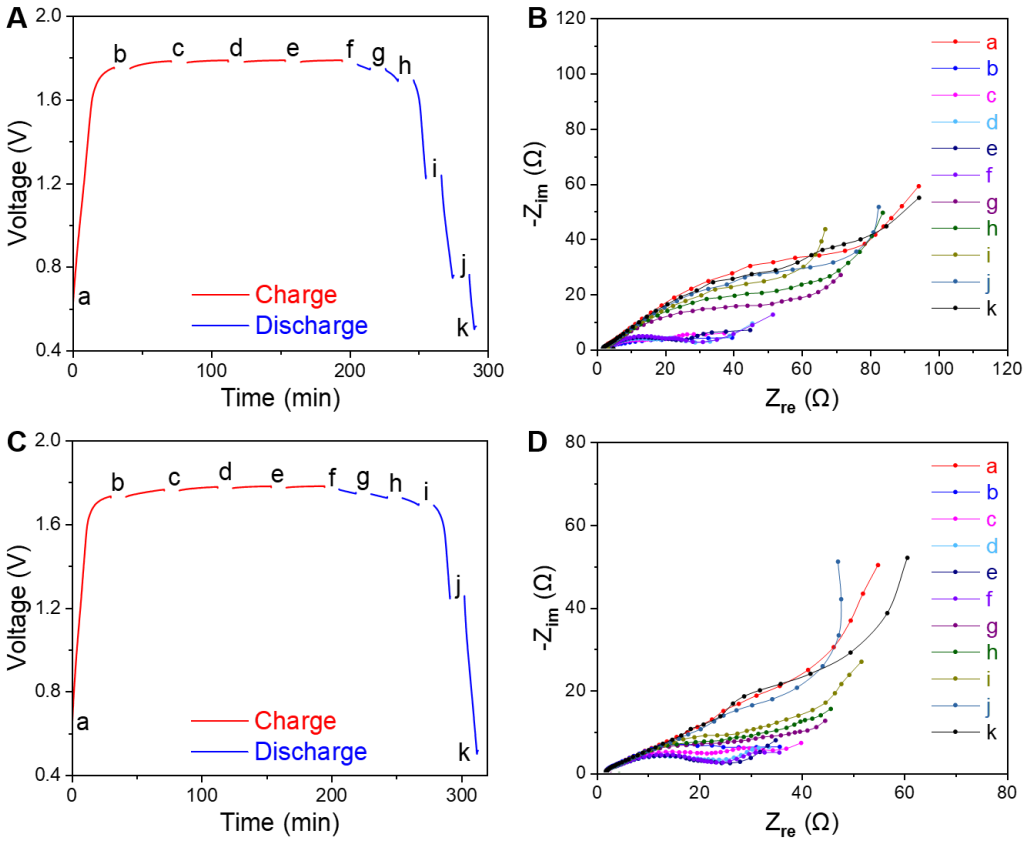

Figure S7. Electrochemical impedance spectroscopy (EIS), related to Figure 2.

EIS of the batteries with activated carbon cathode at different state of charge (SOC) and the corresponding voltage profiles at 100 mA g^{-1} (0.3 mA cm^{-2}) in different electrolytes. (A and B) blank electrolyte. (C and D) MEPBr electrolytes.

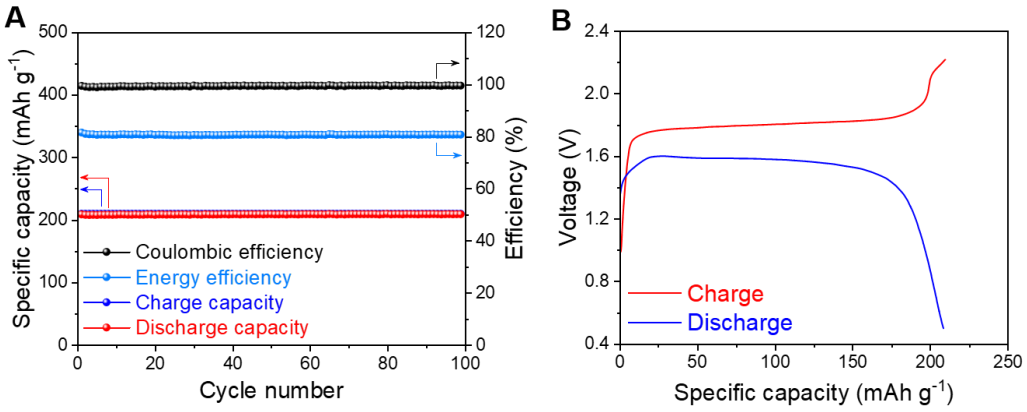

Figure S8. cycling performance, related to Figure 2.

(A) cycling performance of the battery with activated carbon electrode in TPABr electrolyte at 500 mA g^{-1} (1.5 mA cm^{-2}).

(B) the corresponding charge and discharge voltage profiles.

The cut-off voltage is set at 2.2 V.

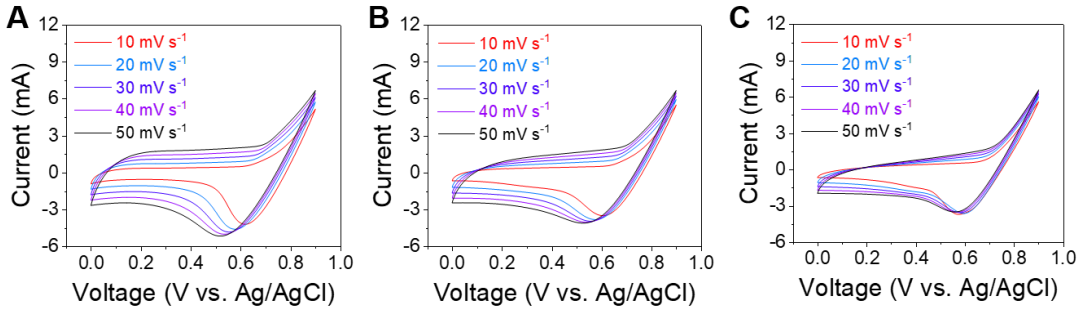

Figure S9. Cyclic voltammogram, related to Figure 2.

Cyclic voltammogram of the zinc-bromine static batteries in different electrolytes at different scan rates. (A) bland electrolyte. (B) MEPBr electrolyte. (C) TPABr electrolyte. Activated carbon electrode served as working electrode, zinc foil as counter electrode and Ag/AgCl electrode as reference electrode.

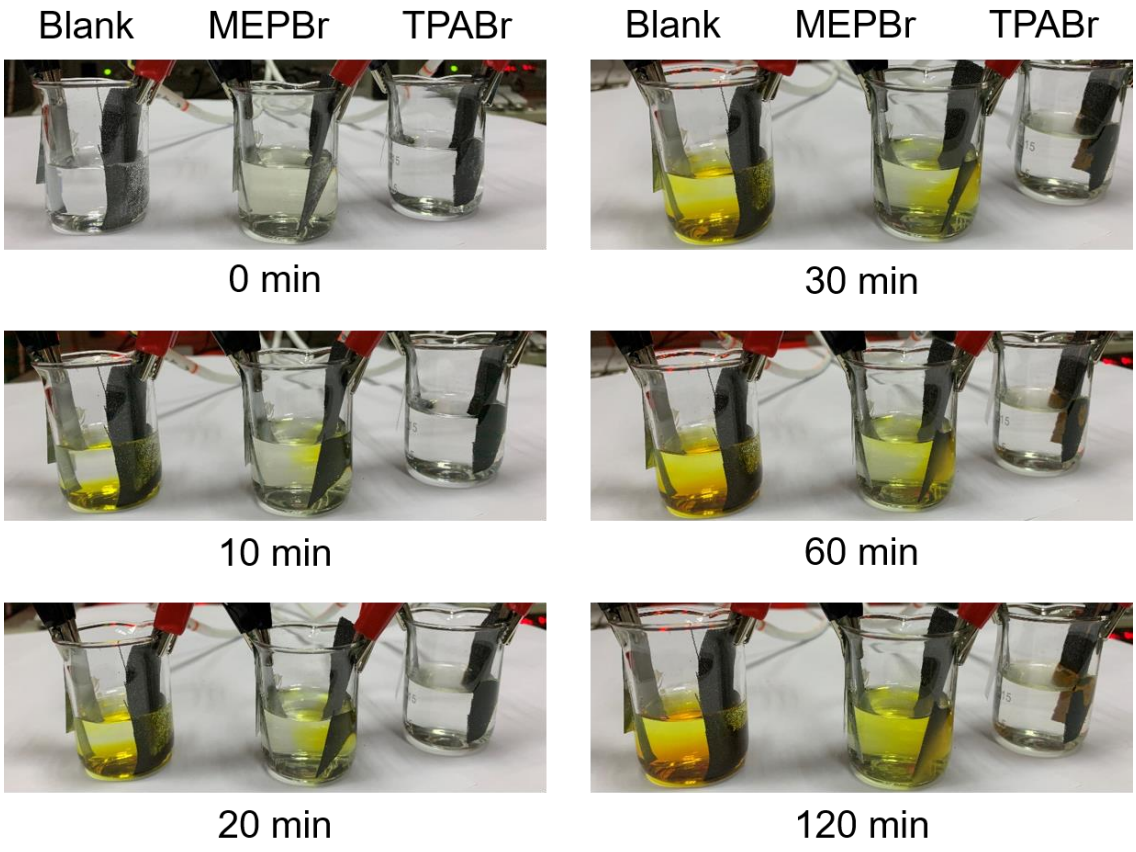

Figure S10. The self-discharge diffusion of bromine species, related to Figure 2.

Photographic images of the transparent cells to show the self-discharge diffusion of the electrochemically generated bromine species. Zinc foil is served as anode and cathode is carbon cloth. The electrolytes are the blank, the MEPBr and the TPABr solutions, respectively. The cells were galvanostatically charged at 20 mA.

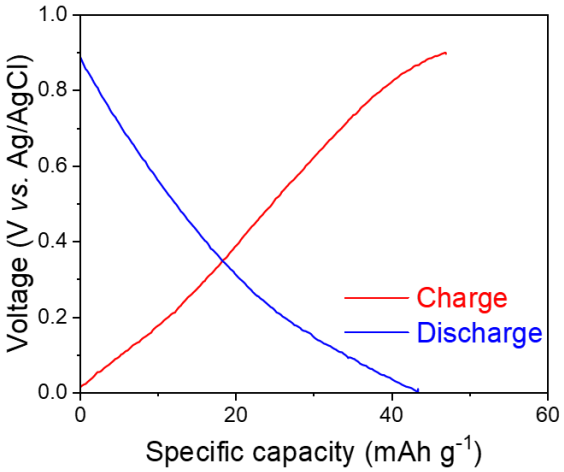

Figure S11. Voltage profile, related to Figure 3.

Voltage profile of the symmetric cell using $ZnCl_2$ solution as electrolyte and CMK-3 as both anode and cathode. Ag/AgCl electrode was served as reference electrode. The cell was tested at a current of 100 mA g^{-1} (0.3 mA cm^{-2}).

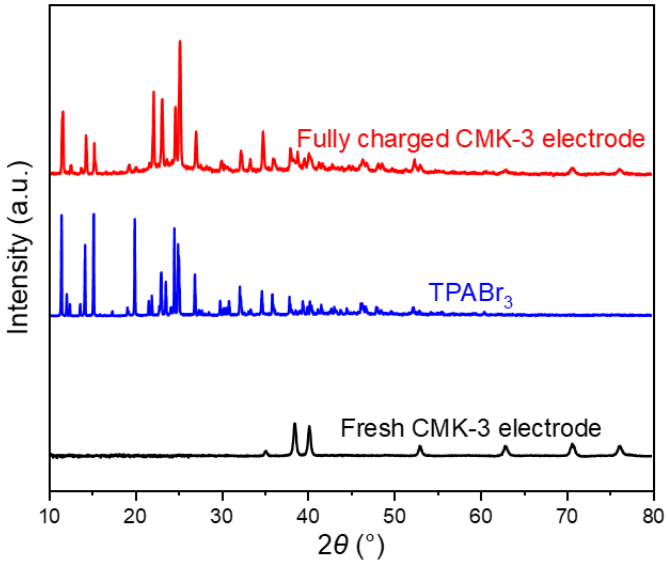

Figure S12. XRD patterns, related to Figure 3.

XRD patterns of the fully charged CMK-3 electrode and fresh CMK-3 electrode.

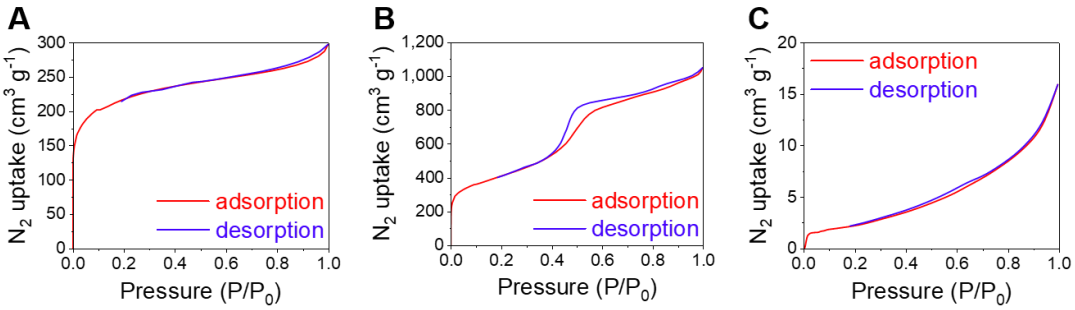

Figure S13. N_2 sorption isotherms, related to Figure 3.

N_2 sorption isotherms of the porous carbon. (A) activated carbon. (B) CMK-3. (C) fully charged CMK-3.

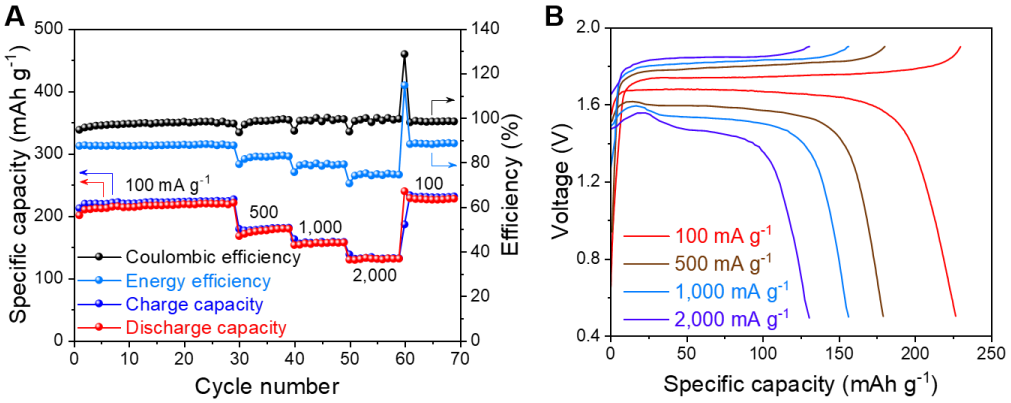

Figure S14. Rate performance, related to Figure 3.

Rate performance of the battery with activated carbon cathode (A) and the corresponding charge and discharge voltage profiles (B).

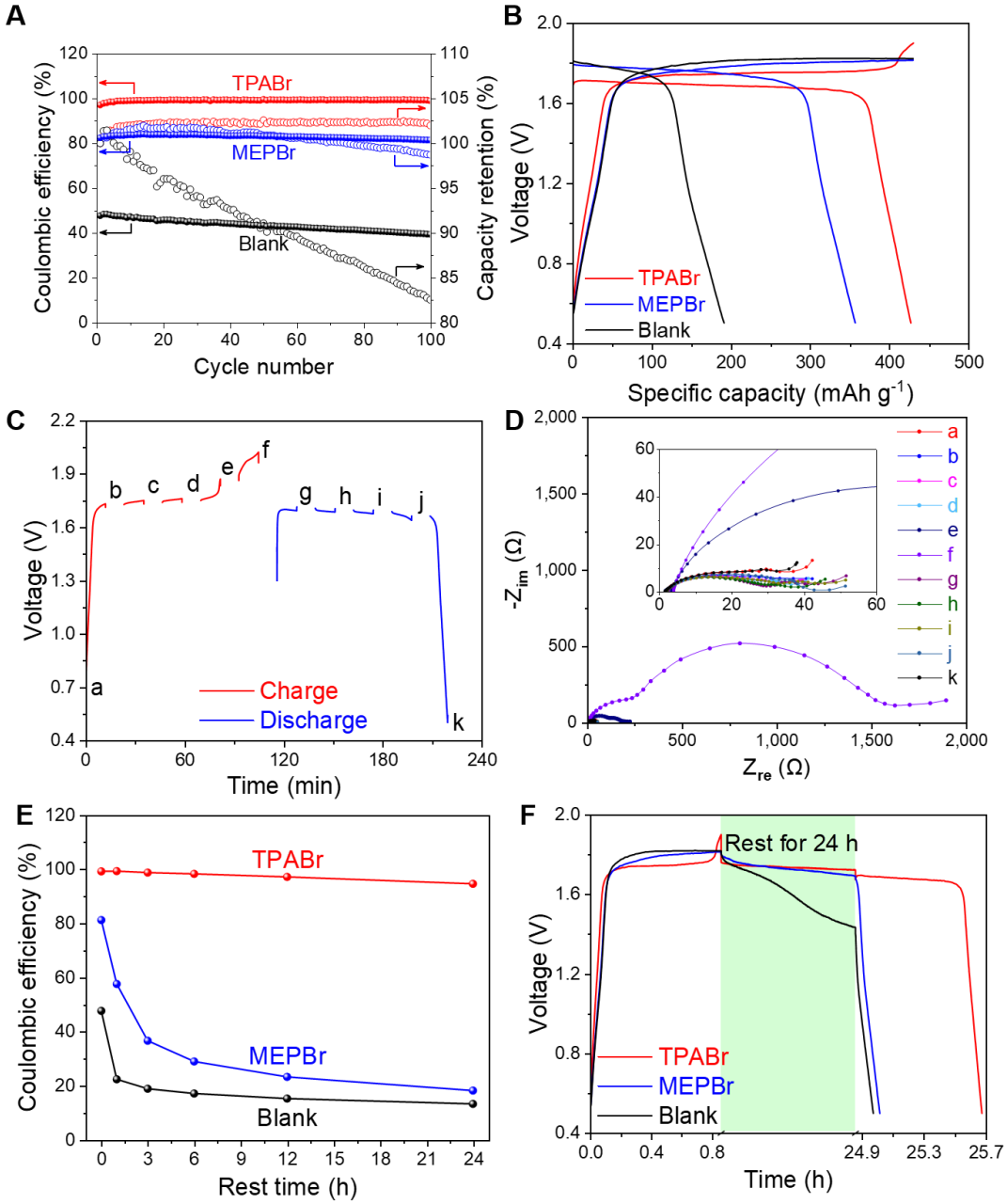

Figure S15. Electrochemical behaviors, related to Figure 3.

Electrochemical behaviors of the batteries with CMK-3 cathode in different electrolytes.

(A) Coulombic efficiencies and capacity retentions at 500 mA g^{-1} (1.5 mA cm^{-2}).

(B) Charge and discharge voltage profiles at 500 mA g^{-1} (1.5 mA cm^{-2}).

(C and D) EIS of the battery with TPABr at different SOC and the corresponding voltage profile at 500 mA g^{-1} (1.5 mA cm^{-2}).

(E) Coulombic efficiencies of the batteries *vs*. rest time between charge and discharge processes.

(F) Voltage profiles with 24 hours of rest between charge and discharge processes.

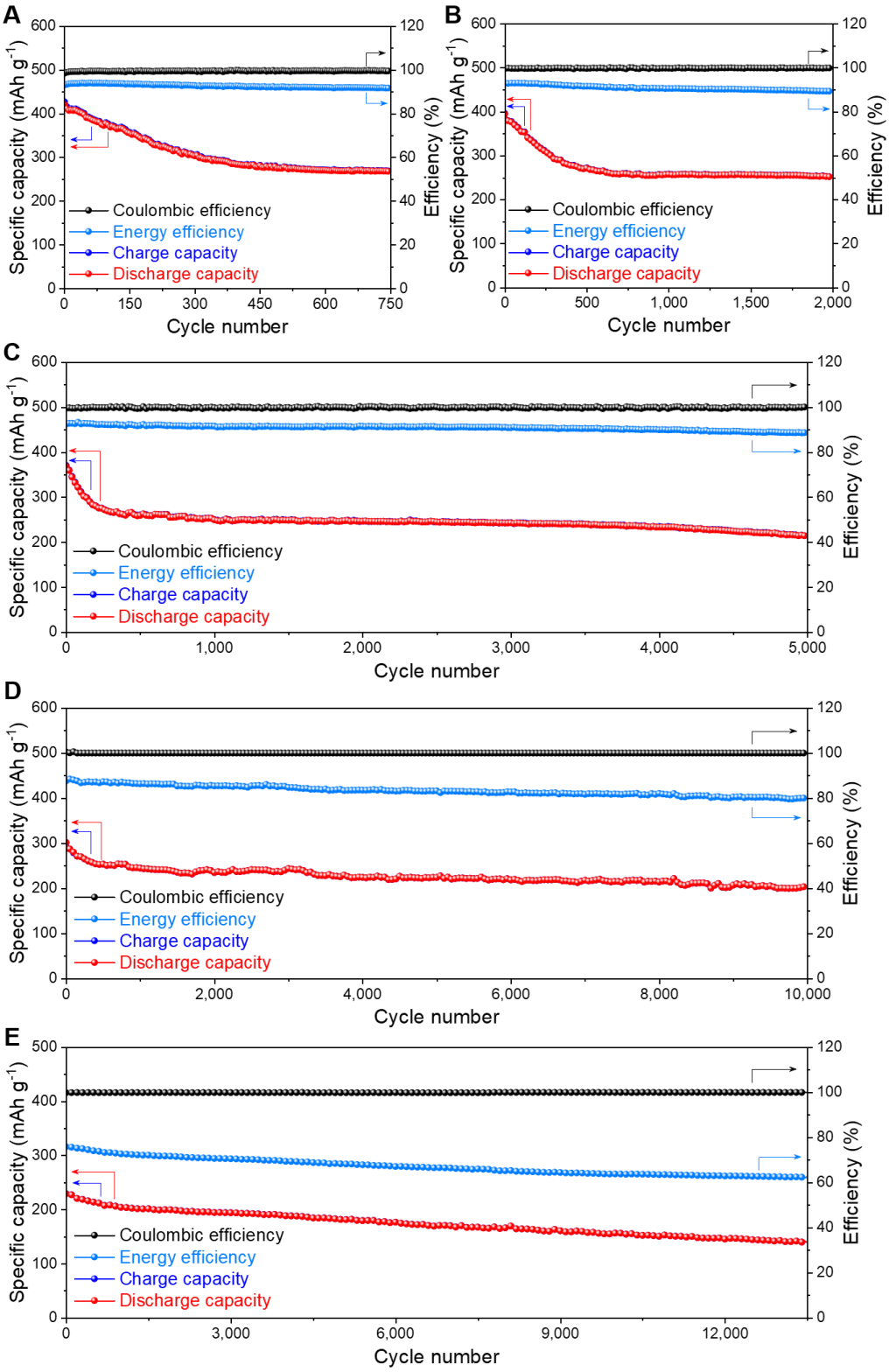

Figure S16. Long-term cycling performances, related to Figure 5.

Long-term cycling performances of the zinc-bromine static batteries with CMK-3 cathodes in the TPABr electrolyte at different current density. (A) 500 mA g^{-1} (1.5 mA cm^{-2}). (B) 1,000 mA g^{-1} (3.0 mA cm^{-2}). (C) 2,000 mA g^{-1} (6.0 mA cm^{-2}). (D) 10,000 mA g^{-1} (30 mA cm^{-2}). (E) 30,000 mA g^{-1} (90 mA cm^{-2}).

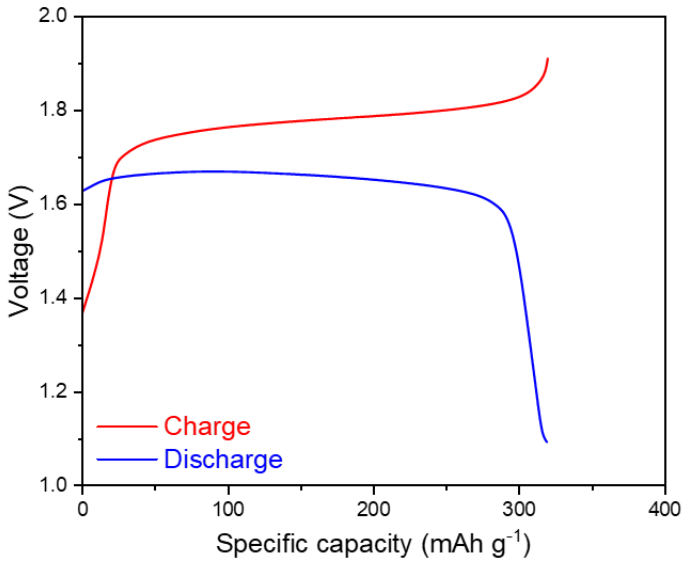

Figure S17. voltage profiles, related to Figure 5.

Charge and discharge voltage profiles of the battery with CMK-3 cathode and Cu foil anode at 5,000 mA g^{-1} (15 mA cm^{-2}).

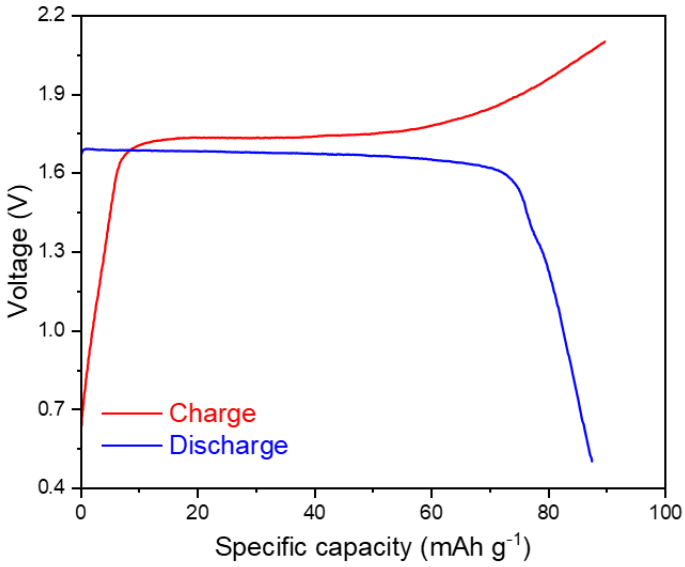

Figure S18. voltage profiles, related to Figure 5.

Charge and discharge voltage profiles of the zinc bromine static battery with $TPABr_3$ electrode at 1.27 mA cm^{-2}.

Transparent Methods

Materials

All reagents and starting materials were used as received without any further purification. The Br_3^- solution is prepared as reported (Evanko et al., 2016). The resulted Br_3^- solution is in dark orange. Then 1 mL H_2O, 1 mL 1 M MEPBr and 1mL 1 M TPABr were added into 3 mL 120 mM Br_3^- respectively, to show the complexations of Br_3^- by MEPBr and TPABr. CMK-3 was synthesized as reported elsewhere (Jun et al., 2000).

Materials characterization

Raman analyses were carried out on a bench Raman dispersive microspectrometer (InVia Reflex, Renishaw) using a laser (wavelength of 532 nm) at frequencies between 1,500 cm^{-1} and 10 cm^{-1}. XRD measurements were carried out on a Bruker D8-Advance powder X-ray diffractometer operating at 40 kV and 30 mA, using Cu-Kα radiation (λ = 0.15405 nm). SEM studies were carried out on a FEI QuANTA 200 environmental SEM instrument. Electrodes were gently washed with deionized water and dried at 60 ℃. Brunauer-Emmett-Teller (BET) measurements were carried out on a JW-BK200C surface area analyzer operating at nitrogen atmosphere with the adsorption temperature of 77 k.

Electrochemical measurements

The activated carbon or CMK-3 powder, poly(vinylidene fluoride) (PVDF) and super P were mixed in dimethylformamide (DMF) with a mass ratio of 8 : 1 : 1. Then the slurry was cast on a titanium foil followed by drying for 12 h in air at 60 ℃. The average mass loading of the carbon in the electrode is 3.0 mg cm^{-2}. As for the $TPABr_3$ electrode, the mass ratio of $TPABr_3$, CMK-3, PVDF and Super P is 6.4 : 1.6 : 1 : 1, and its average mass loading is 70 mg cm^{-2}. Zinc foil (0.1 mm thickness) was used as the anode. Glass fiber was placed between the anode and cathode as the separator. Electrochemical studies were performed in PFA-based Swagelok-type cells (1/2 inch diameter). The electrolyte formula is 0.5 M $ZnBr_2$ (blank electrolyte), 0.2 M MEPBr + 0.5 M $ZnBr_2$ (MEPBr electrolyte), or 0.2 M TPABr + 0.5 M $ZnBr_2$ (TPABr electrolyte), and the amount of electrolyte used in a battery is 100 μL. The electrolyte for the $TPABr_3$ electrode is the TPABr electrolyte, and the electrolyte amount is 80 μL. The cells were then galvanostatically charged/discharged on a Land BT2001A battery test system (Wuhan, China) at room temperature. The charge cut-off voltages were set about 0.1 V higher than the charge voltage plateaus, and the discharge cut-off voltages were set at 0.5 V. For the Zn|Zn symmetric cells, we used a protocol of 24 minutes of stripping followed by 24 minutes of plating with a current density of 5 mA cm^{-1} for each cycle. To investigate the zinc stripping/plating efficiencies, copper foil is used as the counter electrode. Zinc is plated on Cu foil at 5 mA cm^{-1} for 24 minutes, followed by charging up to 0.5 V at the same current density. The electrochemical impedance spectroscopy (EIS) was performed on a VSP-3 electrochemical workstation (Bio-Logic, France) using a 100 μA perturbation with a frequency range of 10 mHz to 1 MHz. Cyclic voltammetry measurements were performed on a VSP-3 electrochemical workstation (Bio-Logic, France) in a three-electrode cell with a Ag/AgCl reference electrode. The scanning voltage range was set from 0 to 0.9 V at scan rates various from 10 to 50 mV s^{-1}.

Supplemental References

Evanko, B., Yoo, S.J., Chun, S.E., Wang, X.F., Ji, X.L., Boettcher, S.W., and Stucky, G.D. (2016). Efficient Charge Storage in Dual-Redox Electrochemical Capacitors through Reversible Counterion-Induced Solid Complexation. J. Am. Chem. Soc. *138*, 9373-9376.

Jun, S., Joo, S.H., Ryoo, R., Kruk, M., Jaroniec, M., Liu, Z., Ohsuna, T., and Terasaki, O. (2000). Synthesis of new, nanoporous carbon with hexagonally ordered mesostructure. J. Am. Chem. Soc. *122*, 10712-10713.